



저작자표시-비영리-변경금지 2.0 대한민국

이용자는 아래의 조건을 따르는 경우에 한하여 자유롭게

- 이 저작물을 복제, 배포, 전송, 전시, 공연 및 방송할 수 있습니다.

다음과 같은 조건을 따라야 합니다:



저작자표시. 귀하는 원저작자를 표시하여야 합니다.



비영리. 귀하는 이 저작물을 영리 목적으로 이용할 수 없습니다.



변경금지. 귀하는 이 저작물을 개작, 변형 또는 가공할 수 없습니다.

- 귀하는, 이 저작물의 재이용이나 배포의 경우, 이 저작물에 적용된 이용허락조건을 명확하게 나타내어야 합니다.
- 저작권자로부터 별도의 허가를 받으면 이러한 조건들은 적용되지 않습니다.

저작권법에 따른 이용자의 권리는 위의 내용에 의하여 영향을 받지 않습니다.

이것은 [이용허락규약\(Legal Code\)](#)을 이해하기 쉽게 요약한 것입니다.

[Disclaimer](#)

Doctor of Philosophy

**ATHERMAL EFFECT OF ELECTRIC CURRENT DURING  
ELECTRICALLY ASSISTED RAPID ANNEALING  
&  
ELECTRICALLY ASSISTED PRESSURE JOINING**

The Graduate School of the University of Ulsan

School of Mechanical Engineering

**Thi Anh Nguyet Nguyen**

**ATHERMAL EFFECT OF ELECTRIC CURRENT DURING  
ELECTRICALLY ASSISTED RAPID ANNEALING**

**&**

**ELECTRICALLY ASSISTED PRESSURE JOINING**

Advisor: **Sung-Tae Hong**

A Dissertation

Submitted to the Graduate School of the University of Ulsan

in Partial Fulfillment of the Requirements

for the Degree of

Doctor of Philosophy

by

**Thi Anh Nguyet Nguyen**

School of Mechanical Engineering

University of Ulsan, Korea

November 2021

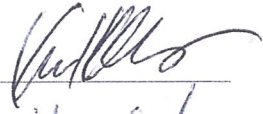
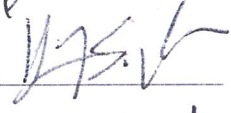

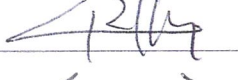

**ATHERMAL EFFECT OF ELECTRIC CURRENT DURING  
ELECTRICALLY ASSISTED RAPID ANNEALING**

**&**

**ELECTRICALLY ASSISTED PRESSURE JOINING**

This certifies that the dissertation of

**THI ANH NGUYET NGUYEN** is approved by

<u>Committee Chairman:</u>	<u>Prof. Koo-Hyun Chung</u>	
<u>Committee Member:</u>	<u>Prof. Sung-Tae Hong</u>	
<u>Committee Member:</u>	<u>Prof. Dong-Kyu Kim</u>	
<u>Committee Member:</u>	<u>Prof. Doo-Man Chun</u>	
<u>Committee Member:</u>	<u>Dr. Moon-Jo Kim</u>	

School of Mechanical Engineering

University of Ulsan, Korea

November 2021

Thi Anh Nguyet Nguyen

©

2021

---

All Rights Reserved

## **ABSTRACT**

First, annealing is one of the unavoidable key processes in many metal forming operations. In conventional annealing, the material is heated to the target temperature during a specific period in a furnace to produce refined grains, to induce softness, to relieve internal stresses, and to improve mechanical properties, depending on the following application. However, in general, conventional annealing using a furnace is time-consuming, requires large space for equipments, and consequently increases the manufacturing cost. To overcome the drawbacks of conventional annealing, electrically assisted (EA) annealing, in which the material is heated to the annealing temperature by an electric current during a relatively short period, has been suggested as a promising alternative annealing technique. In recent years, various studies have been conducted on electrically assisted manufacturing (EAM) utilizing a combination of thermal (resistance heating) and athermal effects of electric current. EA annealing, which is one of EAM methods, also uses the combination of thermal and athermal effects of electric current to enhance the efficiency of the process. The quantification of the thermal and athermal contributions of electric current in EAM can be challenging. A few studies have successfully described the electric current effect in terms of thermal effect only without considering the athermal effect. However, consideration of the athermal effect is generally necessary to thoroughly describe the mechanical or microstructural behaviors under an electric current. Therefore, to design a commercialization ready EA annealing process, the athermal contribution of electric current during the process needs to be properly assessed. Herein, the athermal contribution of electric current during EA rapid annealing (or simply, EA

annealing) with a subsecond duration is evaluated by conducting comparative experiments of EA annealing and rapid induction heat treatment (IHT).

Second, metals are the most widely used materials for fabrication of products. Metal joining, as one of the key manufacturing technologies, is used extensively in production and plays predominant roles in manufacturing industry. Electrically assisted pressure joining (EAPJ) is one of the electrically assisted manufacturing (EAM) techniques. EAM is a new concept for manufacturing processes that utilize the electroplasticity of metals and their alloys to improve productivity, efficiency, and quality. EAPJ using resistance heating as a heat source is a solid state joining without melting or solidification. In this dissertation, the feasibility and effectiveness of EAPJ on single and multi-layers metal sheets are investigated.

In the present work in Chapter III, we investigate the feasibility of EAPJ of CrMnFeCoNi HEA to produce a sound solid-state joint at a temperature substantially lower than its melting point and the effect of an applied electric current pattern on the microstructural change in Joining Zones (JZs). And in chapter IV, we experimentally investigate the EAPJ of thin, cold-rolled Al-clad Al sheets developed for BEV battery casing applications. In EAPJ, an electric current and a compressive load with a constant displacement rate are simultaneously applied to the Al-clad Al sheets. Microstructure analysis and mechanical tests are performed on the EAPJed specimen to investigate the effectiveness of EAPJ.

## ACKNOWLEDGMENTS

First of all, I would like to express the most profound appreciation to my advisor, Professor Sung-Tae Hong, for his guidance, encouragement, suggestion, and very constructive criticism, which have contributed immensely to the evolution of my ideas on the papers and project work. Professor Sung-Tae Hong taught me how to think carefully and deeply in research to touch the level of a doctor. From my heart, he is an important person who gives me a chance to study abroad and conquer my dream. Without his support and guidance, this dissertation would not have been possible to complete on time.

I particularly want to thank Professor Heung Nam Han and his students, Micro-Mechanics & Material Processing Design Lab, for their help and valuable discussions during my studies. It is my pleasure to collaborate with Dr. Min-Gu Jo and Mr. Ho-Wook Choi from Seoul National University for a very valuable distribution of our papers to complete our two papers.

Also, I gratefully acknowledge LG company, SW company, INJIN company and the Korean government for the financial and technical support that allowed me to do this works. It is my pleasure to acknowledge the rest of my committee, Professors Doo-Man Chun, Dong-Kyo Kim, Koo-Hyun Chung, and Dr. Moon-Jo Kim.

In addition, a thank you to Professor Seung-Tae Choi from Chung-Ang University in Seoul, who introduced me to Professor Sung-Tae Hong and give me a chance to study abroad.

I am indebted to all colleagues in the Advanced Engineering Materials Lab, University of Ulsan, especially Dr. Trung Thien Nguyen, Dr. Viet Tien Luu, Mr. Van Loi Tran, Dr. Kieu Anh Dinh, Mr. Thanh Thuong Do, Mr. Shengwei Zhang, Mr. Mondal Mounarik, Mr. Soumya,



Mr. Gao Kun for their support. I will never forget our great moments and valuable discussion during more than five years in Korea.

I am incredibly grateful to my parents, sisters, brothers, parents-in-law and all of my friends for their encouragement, caring, sacrifices for educating, and support through several years. My special thanks go to my husband, Ngoc Duong Nguyen, who always beside me to encourage, support, mobilize to pursue my dream patiently. Last but not least, I would like to thank my son, NiNo Nguyen, who came into my life at a special time.

Thi Anh Nguyet Nguyen

## TABLE OF CONTENT

<b>ABSTRACT .....</b>	<b>i</b>
<b>ACKNOWLEDGMENTS.....</b>	<b>iii</b>
<b>TABLE OF CONTENT .....</b>	<b>v</b>
<b>LIST OF FIGURES.....</b>	<b>viii</b>
<b>LIST OF TABLES.....</b>	<b>xi</b>
<b>CHAPTER I.....</b>	<b>1</b>
<b>INTRODUCTION .....</b>	<b>1</b>
1.1 ELECTRICALLY ASSISTED ANNEALING .....	1
1.2 ELECTRICALLY ASSISTED PRESSURE JOINING .....	4
REFERENCES FOR CHAPTER I.....	7
<b>CHAPTER II .....</b>	<b>10</b>
<b>EXPERIMENTAL EVALUATION OF A THERMAL EFFECT OF ELECTRIC CURRENT DURING ELECTRICALLY ASSISTED RAPID ANNEALING.....</b>	<b>10</b>
<b>ABSTRACT .....</b>	<b>10</b>
2.1 INTRODUCTION.....	11
2.2 EXPERIMENTAL SET-UP .....	13
2.3 RESULTS AND DISCUSSIONS .....	17

2.4 CONCLUSIONS .....	25
REFERENCES FOR CHAPTER II .....	26
<b>CHAPTER III</b> .....	31
<b>ELECTRICALLY ASSISTED SOLID-STATE JOINING OF CrMnFeCoNi HIGH-ENTROPY ALLOY</b> .....	31
ABSTRACT .....	31
3.1 INTRODUCTION .....	32
3.2 EXPERIMENTAL SET-UP .....	34
3.3 RESULTS AND DISCUSSIONS .....	38
3.4 CONCLUSION .....	46
ACKNOWLEDGEMENT .....	47
REFERENCES FOR CHAPTER III .....	48
<b>CHAPTER IV</b> .....	51
<b>ELECTRICALLY ASSISTED PRESSURE JOINING OF ALUMINIUM CLAD ALUMINUM ALLOY</b> .....	51
ABSTRACT .....	51
4.1 INTRODUCTION .....	52
4.2 EXPERIMENTAL SET-UP .....	55
4.3 RESULTS AND DISCUSSIONS .....	59

4.4 CONCLUSIONS .....	69
ACKNOWLEDGEMENT .....	70
REFERENCES FOR CHAPTER IV .....	71
<b>CHAPTER V</b> .....	<b>76</b>
<b>CONCLUSIONS AND PROJECT WORK</b> .....	<b>76</b>
5.1 CONCLUSIONS .....	76
5.2 INDUSTRIAL APPLICATION .....	79
5.2.1. EA flattening of 304 sheets .....	79
5.2.2. Kimchi Container Bright Annealing.....	81
5.2.3. EAPJ of Al-clad Al sheets (apply for Battery Case) .....	83

## LIST OF FIGURES

Fig. 2.1. The schematic of (a) specimen preparation process and (b) EA experimental set-up	15
Fig. 2.2. Temperature profile of specimens at different temperatures by (a) EA annealing and (b) IHT .....	17
Fig. 2.3. The peak temperature during EA annealing.....	18
Fig. 2.4. X-ray diffraction patterns in the range of 35-105° of (a) EA annealed and (b) IHT specimens at different temperatures .....	19
Fig. 2.5. Dislocation density of cold-rolled, EA annealed, and IHT specimens at different temperatures.....	19
Fig. 2.6. FWHM profile in the range of 35-105° of EA and IHT annealed specimens at.....	20
Fig. 2.7. Dislocation density of cold rolled, EA, and IHT annealed specimens at different annealed temperatures .....	21
Fig. 3.1. (a) Geometry of specimen for tensile-shear tests for EAPJ, (b) schematic of the experimental set-up for EAPJ, (c) experimental conditions for applied current and compressive displacement, and (d) measured temperature history during EAPJ .....	35
Fig. 3.2. (a) Typical cross-section of EAPJ collage. (b) high magnification (x3000) SEM-EDS element maps (Cr, Mn, Fe, Co, and Ni) of joining center with C-IV current pattern (yellow box region in Fig. 3.2(a)) and ND IPF map from JZ to BM with C-II current pattern (marked as a blue rectangle in Fig. 3.2(a)) .....	38
Fig. 3.3. ND IPF maps of JZ centers: (a) C-I, (b) C-II, (c) C-III, and (d) C-IV .....	40

Fig. 3.4. (a) Vickers hardness profile at 500 $\mu\text{m}$ intervals in cross-section of EAPJ joint along with the blue dots in the inset and (b) tensile-shear test results of the non-REX (C-I) and full REX (C-IV) EAPJ specimens.....	41
Fig. 3.5. (a) The experimental and simulated load-displacement curves of the non-REX (C-I), full REX (C-IV) EAPJ specimens and non-joined base metal (C-O) using optimized parameters and the contour maps of von Mises stress (b, d) and equivalent plastic strain (c, e) for JZ and BM of EAPJ specimens at the onset of fracture .....	43
Fig. 3.6. (Supplementary Figure) Finite element models of the uniaxial tensile test for C-I and C-IV .....	44
Fig. 3.7. (Supplementary Figure) KAM map from JZ to BM with C-II current pattern. (marked as a blue rectangle in Fig. 2(a)) .....	44
Fig. 3.8. (Supplementary Figure) ND IPF map from JZ to BM with C-III current pattern .....	45
Fig. 4.1. Optical micrograph of the rolled Al-clad Al sheet used for joining and (b) the .....	55
Fig. 4.2. (a) Schematic of the experimental set-up and (b) the design of electrode for EAPJ .	56
Fig. 4.3. Experimental conditions for applied current and compressive displacement .....	58
Fig. 4.4. Compressive displacement, electric current and corresponding load during EAPJ...	60
Fig. 4.5. Process response during EAPJ: (a) measured peak temperature and (b) compressive displacement history .....	61
Fig. 4.6. (a) Typical cross-section of EAPJ collage and (b) higher magnification view of the green box region in (a).....	62
Fig. 4.7. EDS maps of Al and Si particles in (a) as-received and (b) EAPJed Al-clad Al sheets .....	63
Fig. 4.8. SEM micrographs of (a) the EAPJ region and (b) a magnified view of the region ...	63

Fig. 4.9. (a) EBSD locations marked in the OM image of the as-received material (core (1),	64
Fig. 4.10. Misorientation-angle distribution chart of (a) AA3003 before EAPJ, (b) AA3003.	65
Fig. 4.11. Vickers hardness profile of the cross-section of a EAPJed specimen along with the blue dashed line in the inset picture .....	66
Fig. 4.12. (a) EAPJed specimen before and after fracture, (b) lap-shear testing result, and (c) the fracture surface of tensile tested specimens.....	67
Fig. 5.1. Schematic and real experimental set-up.....	79
Fig. 5.2. Position of 5 measured points on the tested specimens .....	79
Fig. 5.3. The specimen before and after testing .....	80
Fig. 5.4. The standard deviation before and after EA.....	80
Fig. 5.5. Deviation from the target height of specimen before and after testing.....	81
Fig. 5.6. The experimental set-up for bright annealing by electric current .....	81
Fig. 5.7. The product after bright annealing by electric current.....	82
Fig. 5. 8. The experimental set-up for battery case joining by EAPJ.....	83
Fig. 5. 9. The working area for each joint .....	84
Fig. 5. 10. The product after EAPJ.....	84

## LIST OF TABLES

Table 2.1. Chemical composition of Al 1050 aluminum alloy .....	13
Table 2.2. The corresponding peak temperatures of five different current densities in EA.....	15
Table 3.1. The electric current conditions for EAPJ .....	36
Table 3.2. The material parameters of Swift equation for BM and JZ.....	42
Table 4.1. Chemical compositions (wt %) of Al-clad Al sheets .....	56
Table 4.2. Compressive displacement and electric current conditions for EAPJ.....	58
Table 4.3. Precipitates inside and in the vicinity of the clad layer's joining area, as marked P1 – P5 in Fig. 4.8(b).....	67



# CHAPTER I

## INTRODUCTION

### 1.1 ELECTRICALLY ASSISTED ANNEALING

The enhancement of manufacturing processes through the application of electricity, in the form of direct current or electric fields, is known as Electrically Assisted Manufacturing (EAM). EAM controls the mechanical properties and microstructure of metals by applying electric current. Current can be applied to a process in various ways, including Alternating Current (AC) or Direct Current (DC), continuous current application or pulsed current application, and varying levels. In EAM, the amount of current applied to a part is typically given as current density ( $A/mm^2$ ), representing the amount of current flowing through the cross-section of the part [1]. In the investigation of electrically assisted manufacturing, noticeable effects of electric current on the microstructure of metals also have been discussed. Many researchers have reported that the applied electric current during deformation drastically affects the material properties such as yield stress, flow stress and elongation. The effect of EAM phenomenon was first reported by Machlin et al. [2] in 1959. According to Machlin, applying an electric current affects flow stress, ductility and yield strength of brittle rock salt. Besides, Roth et al. [3] reported studies that achieved nearly 400% tensile elongation of aluminum 5754 alloys. Regarding rolling, Zhang et al. [4] reported that twins in the microstructure of a rolled AZ91 magnesium alloy were eliminated and a homogeneous fine grain structure was achieved by dynamic electropulsing. Also, Yu et al. [5] reported on microstructure refinement in electropulse induced cold-rolled medium carbon low alloy steels.

Kim et al. [6] analyzed the microstructure changes after applying electric current during uniaxial tension and found that the electric current itself, rather than the Joule heating effect, was the dominant reason of annealing. Moreover, many studies have reported that the changes in the microstructure of materials could be controlled and accelerated by applying electric current with high density to the material without deformation [7-14].

For the conventional process, it needs large area for heating furnace, while it needs relatively small space for power supply in EAM. Also, it needs excess time to heat up the furnace and materials with additional excess energy to maintain the temperature of the furnace and mold. However, the EAM can heat up the materials with a rapid heating with no need to maintain temperature of furnace and mold. Therefore, it is possible to save the cost in space and energy by applying EAM compared to the conventional processes. Moreover, since EAM is expected to be carried out at relatively lower temperatures, the common problems of the conventional process such as thermal stress, warp, and low controllability of tolerance can be minimized. Therefore, the EAM is a cost-effective and energy-saving manufacturing process that also enhances the quality of products. Furthermore, if only the electrode is properly designed for each process, the EAM can be applied to various processes so that it will be considered to be potential applications in manufacturing processes. To the present time, more and more researches on these EAM phenomena have been conducted. However, it needs to be noted that under certain process conditions, the athermal effect of electric current, distinct from the effect of resistance heating, was observed to be insignificant [15-16].

It has been recognized that there is an athermal effect when applying an electric current. EAM is very promising as next generation process because it can improve process efficiency at lower temperature than traditional thermos mechanical process. However, the

mechanism is not fully understood and needs further consideration. In addition, there is a difficulty in utilizing EAM in the material process because the quantification of the athermal effect has not been established. From this research, fundamental understandings of the athermal effect of electric current were established. The distribution of athermal effect of electric current is investigated based on X-ray diffraction data to compare the performance of the processes. In chapter II, The athermal effect of electric current during electrically assisted (EA) annealing was assessed by comparing the performances of EA annealing and induction heat treatment (IHT), using aluminum alloy specimens with a high dislocation density from cold rolling. This experimentally demonstrates reports that the performance of EA annealing clearly surpasses that of IHT in a certain temperature range. However, at higher temperatures, the thermal effect alone is able to induce nearly complete annihilation of dislocation density, thus, the practical advantage of EA annealing may diminish. Through this study, the athermal effect of electric current is quantified.

## 1.2 ELECTRICALLY ASSISTED PRESSURE JOINING

EAM is a new metal manufacturing technique which can enhance formability of metal alloys during deformation and reduce spring-back after deformation [17]. In this method, electric current is directly applied to a metal specimen during deformation. The effect induced by electric current during deformation has been defined as electroplasticity, which has been attributed to some hypotheses. Firstly, localized atomic-level resistive heating effects are enhanced by the resistivity of the material, for example, electrons scatter off of interfacial defects within the lattice, such as voids, impurities, grain boundaries [18]. This heating occurs on the atomic level (within the metal's lattice), and although this contributes toward the overall heating of the workpiece, this temperature increase is not the same as the bulk temperature increase that is witnessed at the part's surface (known as global or bulk heating) [17]. Specifically, the bulk temperature of a metal is the result of all the atomic-level heating locations. This effect expands the local lattice and allows for easier dislocation motion (i.e., plastic deformation) by the way of enhanced diffusion [17]. Secondly, direct dislocation–electron interaction takes place as the flowing electrons impact the dislocation lines, assisting in “pushing” the dislocation lines and further enhancing plastic deformation and material ductility [19]. This can be used to explain why the temperature of an EA forming test, where electricity is applied during deformation, is less than a stationary electrical test, where the electricity is applied when no deformation takes place.

Electrically assisted pressure joining (EAPJ) is one of the EAM. EAPJ using resistance heating as a heat source is a solid state joining without melting or solidification. In this dissertation, the feasibility and effectiveness of EAPJ on similar and dissimilar metal materials

are investigated. EAPJ is a solid-state joining without melting in contrast to the resistance spot welding, which is one of fusion joining technologies with melting and solidification. In comparison to conventional pressure joining, EAPJ has several technical advantages. The workpieces can be heated rapidly and locally. As a result, the process time can be reduced and unnecessary thermal effects on the workpiece can be minimized. Also, the joining apparatus can be significantly simpler and cost-effective due to the need for a heating furnace is eliminated.

However, little research has been done in EAPJ so far. The studies on EAPJ of metal alloys are mostly focused on very thin foils. Ng et al. [20] applied electrically assisted roll bonding process to bond 127  $\mu\text{m}$  aluminum sheet to 127  $\mu\text{m}$  aluminum or 127  $\mu\text{m}$  copper sheets. Xu et al. [21] successfully joined SUS316L foils with thickness of 100  $\mu\text{m}$  using EAPJ. Peng et al. [22] conducted EAPJ of brass to brass (CuZn40) and SUS316L to SUS316L with different thicknesses of 100  $\mu\text{m}$  and 150  $\mu\text{m}$ . In practice, except thin foil specimens, EAPJ can be also used to join structural plates and bulk workpieces. Especially, in the joining of bulk components, EAPJ also provides technical advantages over friction joining that is usually considered for joining cylindrical parts. For example, friction joining requires a relatively expensive and complex brake system since the rotation of a workpiece must be stopped completely and rapidly for successful joining [23]. Also, there is no additional frictional heat generated during the actual generation of a solid-state joint since the rotation ceases prior to the final axial compression during friction welding. However, in EAPJ using resistance heating as a heat source, the need for complex rotation and brake systems can be eliminated. Also, since the heating of the interface can be continued during the final axial compression, process optimization is relatively easier. In the present study, EAPJ of high entropy alloy

(chapter III) and EAPJ of aluminium-clad aluminium sheets (Chapter IV) are experimentally investigated. Chapter III to IV are presented as two independent journal papers which have been published.

In chapter III, EAPJ of high entropy alloy is experimental investigated. Equiatomic CrMnFeCoNi high-entropy alloy was joined in solid-state by EAPJ. Cracks and compositional segregation were not found in Joining Zones (JZ). As the applied electric current increased, the microstructure of JZ changed from a deformed and partially recrystallized microstructure to a fully recrystallized one with grain growth. JZ showed sound mechanical properties through the Vickers hardness and uniaxial tension results. EAPJ of high-entropy alloy can overcome the disadvantages of fusion welding.

In chapter IV, a cost-effective and lightweight battery in battery-driven electric vehicles, using Al-clad Al sheet is being considered recently. The EAPJ of bi-layer cold-rolled Al-clad Al thin sheets is experimentally investigated to apply for the battery. Before electric current is applied, the pre-displacement (pre-load) is directly forced to create good contact between two cold-rolled Al-clad Al sheets, thus avoiding sparks that may occur during the joining process. A compressive displacement is then applied to the Al-clad Al sheets to induce plastic deformation of the joint area while a pulsed electric current with varying current density is applied. Microstructure analysis results confirm that the Al-clad Al sheets are successfully joined in solid-state joining at low temperature, which is significantly lower than the melting temperature of selected alloys, within a relatively short time. Furthermore, the mechanical properties through the uniaxial tension and Vickers hardness test are also briefly evaluated. Finally, the conclusion will be given in Chapter V.

## REFERENCES FOR CHAPTER I

- [1] Ruszkiewicz, B. J., Grimm, T., Ragai, I., Mears, L., and Roth, J. T. (September 13, 2017). "A Review of Electrically-Assisted Manufacturing With Emphasis on Modeling and Understanding of the Electroplastic Effect." ASME. J. Manuf. Sci. Eng. November 2017; 139(11): 110801. <https://doi.org/10.1115/1.4036716>
- [2] E.S. Machlin, Applied voltage and the plastic properties of "Brittle" rock salt, J. Appl. Phys. 30(7) (1959) 1109-1110.
- [3] J.T. Roth, I. Loker, D. Mauck, M. Warner, S.F. Golovashchenko, A. Krause, Enhanced formability of 5754 aluminum sheet metal using electric pulsing, Trans. NAMRI/SME. 36 (2008) 405-412.
- [4] D. Zhang, S. To, Y. Zhu, H. Wang and G. Tang, Dynamic electropulsing induced phase transformations and their effects on single point diamond turning of AZ91 alloy, Journal of Surface Engineered Materials and Advanced Technology, 2 (2012) 16-21
- [5] W. P. Yu, R. S. Qin and K. M. Wu, The effect of hot-and cold-rolling on the electropulse-induced microstructure and property changes in medium carbon low alloy steels, Steel Research International, 84 (2013) 443-449
- [6] M.-J. Kim, K. Lee, K.H. Oh, I.S. Choi, H.H. Yu, S.-T. Hong, H.N. Han, Electric current-induced annealing during uniaxial tension of aluminum alloy, Scr. Mater. 75 (2014) 58–61.
- [7] Conrad, H., Karam, N., Mannan, S. and Sprecher, A. (1988). Effect of electric current pulses on the recrystallization kinetics of copper. Scripta metallurgica, 22(2), 235-238.
- [8] Conrad, H., Karam, N. and Mannan, S. (1983). Effect of electric current pulses on the recrystallization of copper. Scripta metallurgica, 17(3), 411- 416.

- [9] Wang, T., Xu, J., Xiao, T., Xie, H., Li, J., Li, T. (2010). Evolution of dendrite morphology of a binary alloy under an applied electric current: An in situ observation. *Physical Review E - Statistical, Nonlinear, and Soft Matter Physics*, 81(4), doi:10.1103/PhysRevE.81.042601.
- [10] Jeong, H. J., Kim, M. J., Park, J. W., Yim, C. D., Kim, J. J., Kwon, O. D. and Han, H. N. (2017). Effect of pulsed electric current on dissolution of Mg 17 Al 12 phases in as-extruded AZ91 magnesium alloy. *Materials Science and Engineering A*, 684, 668-676, doi:10.1016/j.msea.2016.12.103.
- [11] Choi, J., Sung, H. M., Roh, K. B., Hong, S. H., Kim, G. H. and Han, H. N. (2017). Fabrication of sintered tungsten by spark plasma sintering and investigation of thermal stability. *International Journal of Refractory Metals and Hard Materials*, 69, 164-169, doi:10.1016/j.ijrmhm.2017.08.013.
- [12] Y. Estrin, L.S. Tóth, A. Molinari, Y. Bréchet, A dislocation-based model for all hardening stages in large strain deformation. *Acta Mater.* 46 5509- 5522 (1998).
- [13] U.F. Kocks, H. Mecking, Physics and phenomenology of strain hardening: the FCC case. *Prog. Mater. Sci.* 48 171-273 (2003).
- [14] A. S. Krausz, K. Krausz, *Unified Constitutive Laws of Plastic Deformation* (Academic Press, San Diego, 1996)
- [15] T. A. Perkins, T. J. Kronenberger and J. T. Roth, Metallic forging using electrical flow as an alternative to warm/hot working, *Journal of Manufacturing Science and Engineering*, 129 (2007) 84-94.
- [16] B. Kinsey, G. Cullen, A. Jordan and S. Mates, Investigation of electroplastic effect at high deformation rates for 304SS and Ti-6Al-4V, *CIRP Ann. Manuf. Technol.*, 62 (2013) 279- 282.



- [17] Salandro WA, Jones JJ, Bunget C, Mears L, Roth JT (2015) Electrically assisted forming: modeling and control. Springer International Publishing, Switzerland.
- [18] Roth JT, Loker I, Mauck D, Warner M, Golovashchenko SF, Krause A (2008) Enhanced formability of 5754 aluminum sheet metal using electric pulsing. Transactions of the North American Manufacturing Research Institution of SME 36:405–412
- [19] Yao L, Hong C, Yunquo G, Xinbin H (1996) Effect of electric current pulse on superplasticity of aluminum alloy 7475. Transactions of Nonferrous Metals Society of China. 6(1):77–84.
- [20] Nguyen-Tran HD, Oh HS, Hong ST, Han HN, Cao J, Ahn SH, Chun DM (2015) A review of electrically-assisted manufacturing. International Journal of Precision Engineering and Manufacturing-Green Technology 2(4):365-376
- [21] Xu Z, Peng L, Lai X (2014) Electrically assisted solid-state pressure welding process of SS 316 sheet metals. Journal of Materials Processing Technology 214(11):2212–2219
- [22] Peng L, Xu Z and Lai X (2013) An investigation of electrical-assisted solid-state welding/bonding process for thin metallic sheets: Experiments and modeling. Proceedings of the Institution of Mechanical Engineers Part B Journal of Engineering Manufacture 228(4): 582-594
- [23] Kimura M, Suzuki K, Kusaka M, Kaizu K (2017) Effect of friction welding condition on joining phenomena and mechanical properties of friction welded joint between 6063 aluminium alloy and AISI 304 stainless steel. Journal of Manufacturing Processes 26:178-187

**CHAPTER II**

**EXPERIMENTAL EVALUATION OF ATHERMAL EFFECT OF  
ELECTRIC CURRENT DURING ELECTRICALLY ASSISTED RAPID  
ANNEALING**

**ABSTRACT**

The athermal effect of electric current during electrically assisted (EA) annealing was assessed by comparing the performances of EA annealing and induction heat treatment (IHT), using aluminum alloy specimens with a high dislocation density from cold rolling. The dislocation densities after EA annealing and IHT are calculated using X-ray diffraction data to compare the performance of the processes. The performance of EA annealing clearly surpasses that of IHT in a certain temperature range. However, at higher temperatures, the thermal effect alone is able to induce nearly complete annihilation of dislocation density, thus, the practical advantage of EA annealing may diminish.

**Keywords:** Electrically assisted annealing; Electrical pulse treatment; Dislocation density; Athermal effect

## 2.1 INTRODUCTION

Annealing is one of the unavoidable key processes in many metal forming operations. In conventional annealing, the material is heated to the target temperature during a specific period in a furnace to produce refined grains, to induce softness, to relieve internal stresses, and to improve mechanical properties, depending on the following application. However, in general, conventional annealing using a furnace is time-consuming, requires large space for equipments, and consequently increases the manufacturing cost. To overcome the drawbacks of conventional annealing, EA annealing, in which the material is heated to the annealing temperature by an electric current during a relatively short period, has been suggested as a promising alternative annealing technique [1,2].

In recent years, various studies have been conducted on EAM [2-10] utilizing a combination of thermal (resistance heating) and athermal effects [11] of electric current. EA annealing, which is one of EAM methods, also uses the combination of thermal and athermal effects of electric current to enhance the efficiency of the process. Kim et al. [12] showed that electric current can rapidly annihilate the dislocations in a deformed metal and confirmed the existence of athermal effect of electric current by conducting a detailed microstructural analysis. Park et al. [13] also demonstrated that the additional athermal effect of electric current could enhance the performance of EA tempering of automotive products. Their results showed that the performance of EA tempering surpassed that of a conventional tempering process, even with a lower energy and a significantly shorter process time. In addition, Liu et al. [14] reported that a pulsed electric current enhanced the dislocation annihilation during annealing of AZ31B magnesium sheets.

As reported in previous works mentioned above, by utilizing the combination of thermal and athermal effects of electric current, the processing time of EA annealing can be shorter than a few seconds. Consequently, the productivity can be significantly enhanced, while the manufacturing cost decreases. Also, the capability of selective local heating of EA annealing can improve the quality of product by optimizing the size of heat-affected region. These advantages make EA annealing a promising energy-saving green technology. The quantification of the thermal and athermal contributions of electric current in EAM can be challenging [15]. A few studies have successfully described the electric current effect in terms of thermal effect only without considering the athermal effect [16,17]. However, consideration of the athermal effect is generally necessary to thoroughly describe the mechanical or microstructural behaviors under an electric current [18-20]. Therefore, to design a commercialization-ready EA annealing process, the athermal contribution of electric current during the process needs to be properly assessed. Herein, the athermal contribution of electric current during EA rapid annealing (or simply, EA annealing) with a subsecond duration is evaluated by conducting comparative experiments of EA annealing and rapid induction heat treatment (IHT).

## 2.2 EXPERIMENTAL SET-UP

A commercial 1050 aluminum alloy (AA1050, Table 2.1), which contains very few precipitated particles acting as barriers against dislocation mobility, was selected. AA1050 plates with a thickness of 25 mm were cold rolled to 5 mm thick sheets (80% thickness reduction) to introduce a recognizable magnitude of dislocation density. Cylindrical specimens (a diameter of 8 mm; a height of 5 mm) were prepared by wire cutting from the cold-rolled sheet along the thickness of the sheet for the EA annealing and IHT experiments, as described in Fig. 2.1(a). Prior to an experiment, the specimen was slightly polished by silicon carbide grinding paper to flatten its top and bottom surfaces. The specimen was then cleaned by ethanol to remove residual oil from the preparation process.

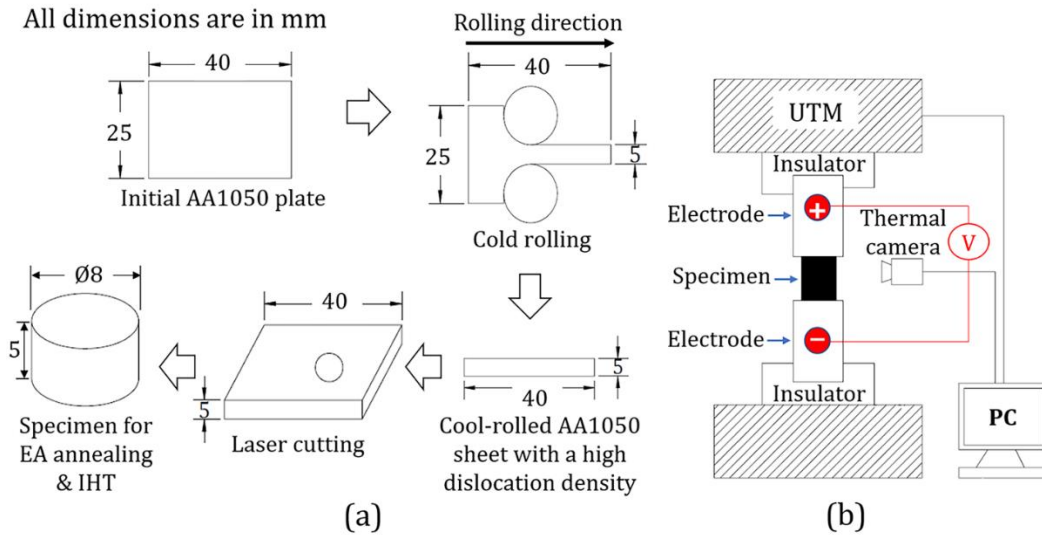
**Table 2.1. Chemical composition of Al 1050 aluminum alloy**

Material	Chemical composition (wt%)							
	Al	Si	Fe	Cu	Mn	Zn	Ti	Others
AA1050	Bal.	0.128	0.135	0.002	0.011	0.001	0.015	0.150

To evaluate the effect of electric current on the dislocation annihilation, specimens were annealed by EA annealing and IHT at the same temperatures for the same heating time. A fixture was custom-made and placed in a programmable universal testing machine, as described in Fig. 2.1(b). To protect the testing machine, a pair of insulators were placed between the electrodes and the specimens. A power supply (SP-1000U, Hyosung, ROK) was employed to generate the electric current. A constant pre-load of 100 N was applied to the specimen to avoid sparking during the experiment by providing firm contact between the electrode and the specimen. In the EA annealing, five different current densities with a fixed duration (0.5 sec), which corresponds to the heating time, were firstly used to induce different

peak temperatures using current density as the control parameter (Table 2.2). One additional current density of  $25 \text{ A/mm}^2$  was later adopted to better describe the trend of experimental results for the region, in which EA annealing showed distinctively different performance compared to IHT. During the EA annealing, the specimen temperature was monitored using an infrared thermal imaging camera (T621, FLIR, Sweden). To accurately measure the temperature, black thermal paint stabilizing the emissivity was applied on a side of the specimen facing the camera.

For conventional annealing by IHT, a rapid induction heating equipment was used to increase the specimen temperature to the peak value reached in the EA annealing in the same heating time of 0.5 sec. Note that the eddy current used in IHT to rapidly heat the specimen is a surface phenomenon [21]. Right after the induction heating, the specimen was cooled by forced air to imitate rapid cooling of EA annealing as much as possible. During IHT, the temperature was measured by a K-type thermocouple at the center of the specimen. Repeatability of the experiment was confirmed by repeating the test at least three times at each test parameter.



**Fig. 2.1.** The schematic of (a) specimen preparation process and (b) EA experimental set-up

**Table 2.2. The corresponding peak temperatures of five different current densities in EA annealing**

Current density (A/mm <sup>2</sup> )	10	20	30	40	50
Peak temperature (°C)	137	226	330	383	412

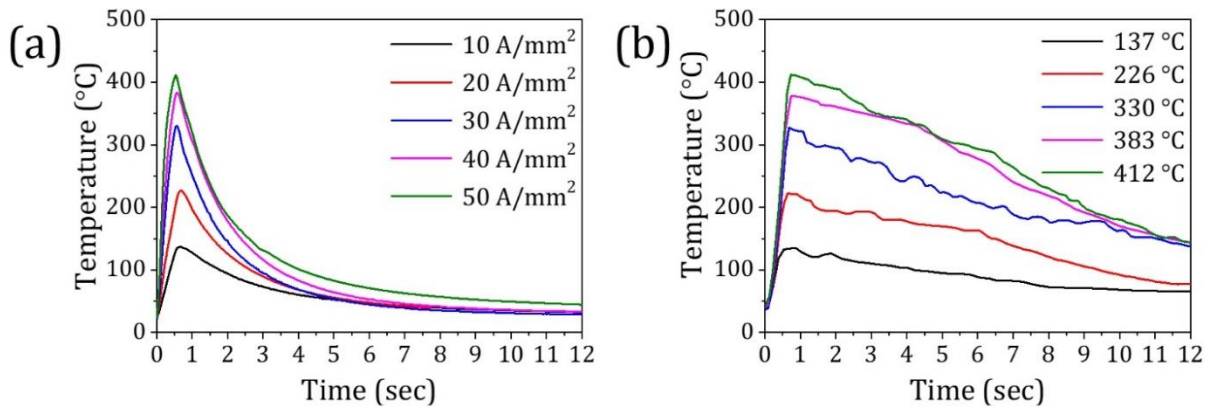
The specimens after EA annealing and IHT were analyzed by X-ray diffraction (XRD, D8–Advance, Bruker Miller Co., Germany) using Cu K $\alpha$  radiation with a 1.51Å wavelength at room temperature (scan range: 35-105°; scan speed: 1°/min). Pseudo-Voigt function [22-23] was used to fit the diffraction peaks. The full width at half maximum (FWHM) from the diffraction peaks of the XRD data for the annealed specimens was then used to estimate the dislocation density by the Williamson-Hall equation [24-25]. Inverse Pole Figure (IPF) maps were constructed using an electron backscatter diffraction (EBSD) system (Hikari EBSD detector with TSL OIM 6.1 software, EDAX/TSL, USA) to obtain microstructural information of the EA annealed and IHT specimens. A micro-Vickers indenter (Duramin-40,

Struers, Denmark) was used for the hardness measurement of the specimens after EA annealing and IHT (load: 2.94 N; dwell time: 10 sec).

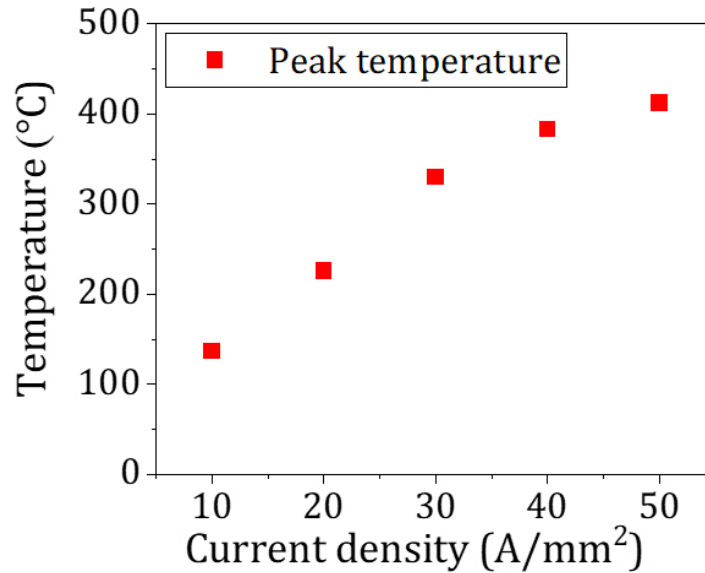


## 2.3 RESULTS AND DISCUSSIONS

For both EA annealing and IHT, the specimen temperature rapidly reached the peak temperature, as shown in Fig. 2.2. Naturally, the peak temperature during EA annealing (137, 226, 330, 383, and 412 °C) increased as the electric current density (10, 20, 30, 40, and 50 A/mm<sup>2</sup>) increased, as shown in Fig. 2.3. The peak temperatures with the electric current densities of 30, 40, and 50 A/mm<sup>2</sup> are in the range of generally known recrystallization temperature for aluminum alloys. Due to the heat transfer through the electrodes, the cooling rate of EA annealing was significantly faster than that of IHT, even though the IHT specimen



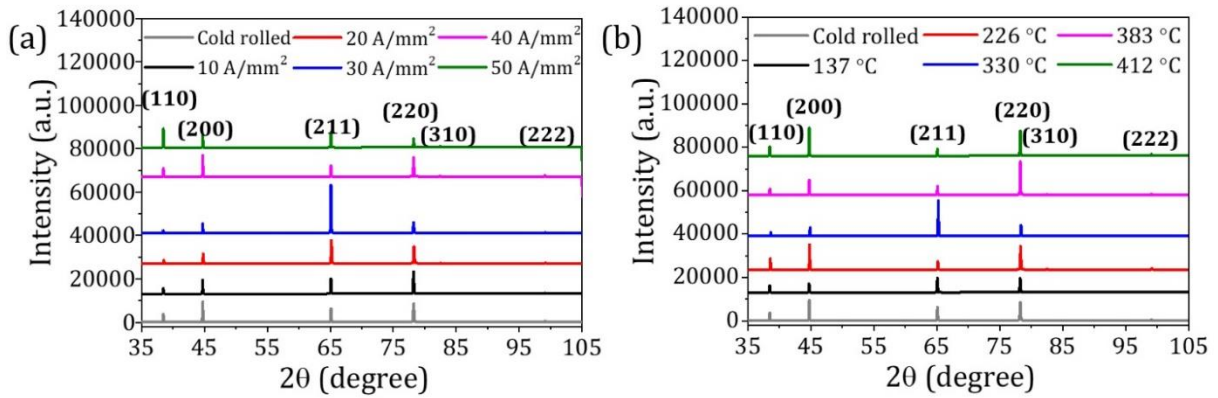
**Fig. 2.2.** Temperature profile of specimens at different temperatures by (a) EA annealing and (b) IHT



**Fig. 2.3.** The peak temperature during EA annealing

was cooled with forced air at 3 MPa, which indicates that the IHT specimen was exposed to elevated temperatures longer than the EA annealed specimen. However, the cooling rate was not considered an effective factor in the present work. As a result, the difference in the energy obtained during cooling for EA annealing and IHT was ignored in the analysis of the result.

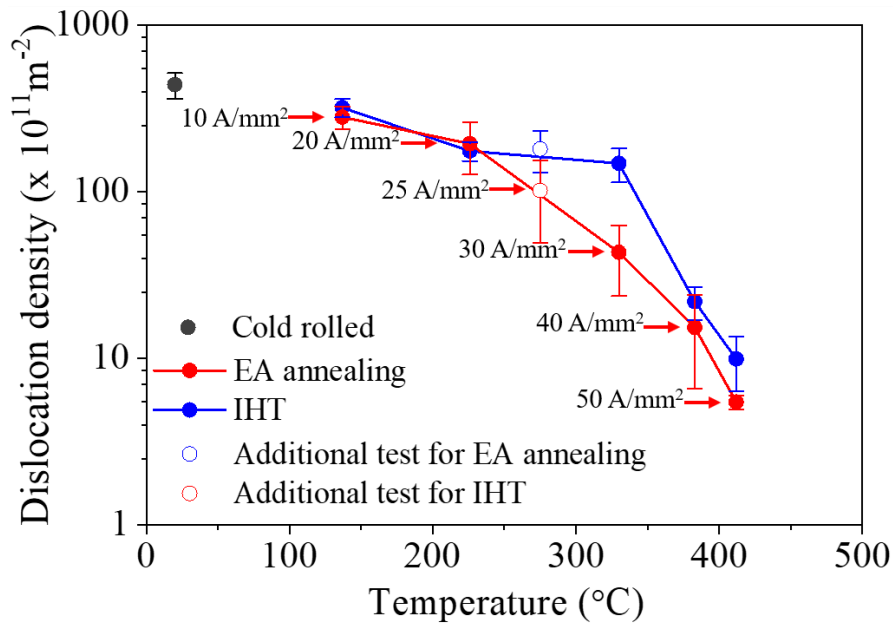
The performances of EA annealing and IHT were quantitatively compared using the remaining dislocation density in the EA annealed and IHT specimens. Fig. 2.4 shows the XRD patterns in the range from 35 to 105° of EA annealed and IHT specimens at different temperatures. The FWHM was obtained from the XRD peaks of EA annealed and IHT specimens, as a function of the Bragg angle of XRD peaks. As mentioned in Kim et al. [12], the change of FWHM indicates the change of dislocation density, since XRD peaks will be broadened if a large amount of lattice defects appears [7,14,26,27].



**Fig. 2.4.** X-ray diffraction patterns in the range of 35-105° of (a) EA annealed and (b) IHT specimens at different temperatures

The FWHM can be expressed by the strain-induced peak broadening using the Williamson–Hall equation [24]:

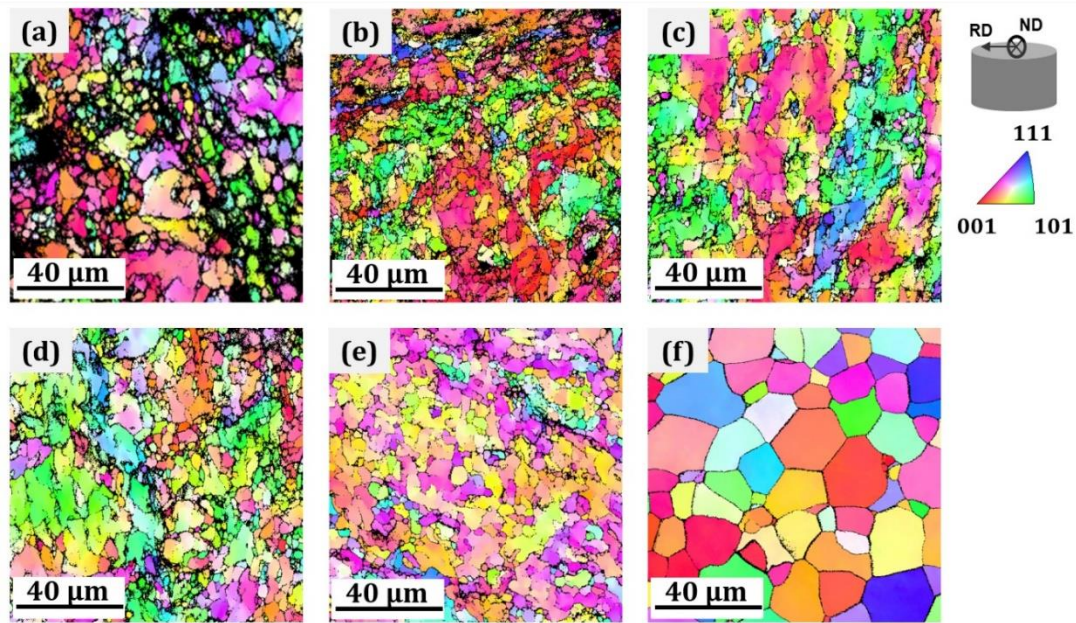
$$\beta \frac{\cos\theta}{\lambda} = \frac{K}{D} + 2\varepsilon_r \frac{\sin\theta}{\lambda} \quad (1)$$



**Fig. 2.5.** Dislocation density of cold-rolled, EA annealed, and IHT specimens at different temperatures

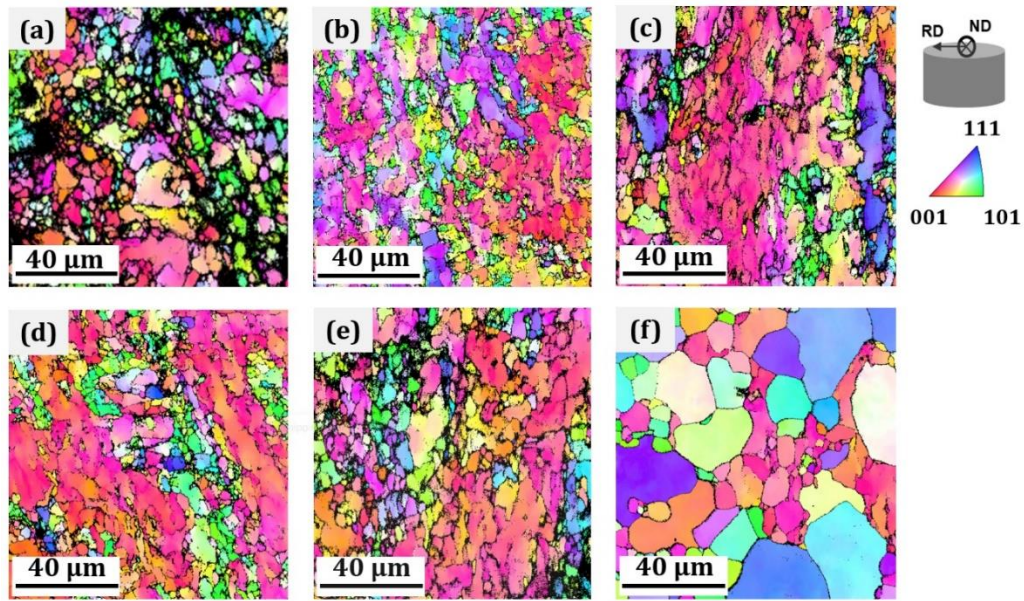
where  $\beta$  is FWHM calculated from the XRD measurement and  $K$  is a dimensionless constant of 0.94. Also,  $\theta$ ,  $D$ , and  $\lambda$  represent the corresponding Bragg angle, the average crystallite size, and the wavelength of the X-ray source, respectively. In addition, the two terms of  $\frac{K}{D}$  and  $2\varepsilon_r \frac{\sin \theta}{\lambda}$  are the grain size-induced peak broadening and strain-induced peak broadening, respectively. Finally,  $\varepsilon_r$  is the micro-strain induced by crystal imperfections. The micro-strain  $\varepsilon_r$  was obtained by a linear fitting of  $2\sin\theta$  (along the x-axis) and  $\beta\cos\theta$  (along the y-axis). From the micro-strain, the dislocation density  $\rho$  was then obtained [28]:

$$\rho = \frac{6\pi E}{G \ln\left(\frac{r}{r_0}\right)} \left(\frac{\varepsilon_r}{b}\right)^2 \quad (2)$$



**Fig. 2.6.** FWHM profile in the range of 35-105° of EA and IHT annealed specimens at

(a) 137°C (b) 226°C, (c) 330°C, (d) 383°C and (e) 412°C.



**Fig. 2.7.** Dislocation density of cold rolled, EA, and IHT annealed specimens at different annealed temperatures

where  $E$  is the elastic modulus (70.3 GPa),  $G$  is the shear modulus (25.9 GPa),  $r$  and  $r_0$  are outer and inner cut off radii ( $\ln\left(\frac{r}{r_0}\right) = 4$ ), and  $b$  is the Burgers vector (0.286 nm).

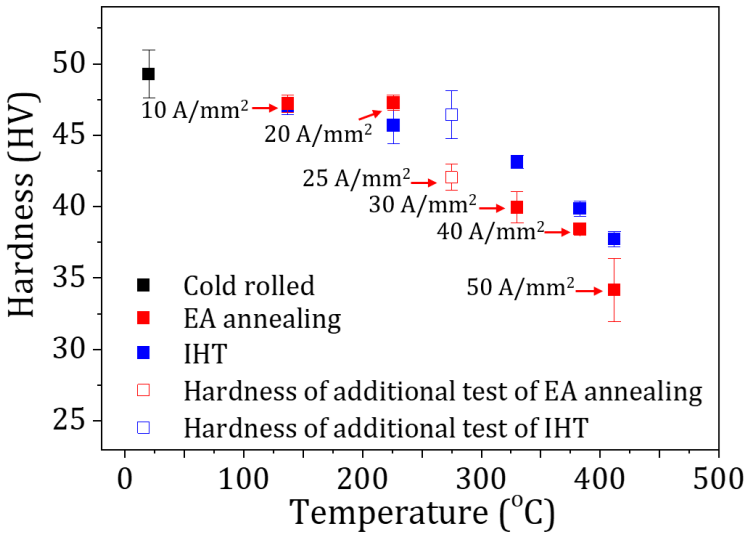
Using Eq. (2), the dislocation densities of the EA annealed and IHT specimens were obtained at each current density or annealing temperature (Fig. 2.5). As expected, the dislocation density in both cases decreased as the annealing temperature increased (the annealing was enhanced). For the relatively low temperatures (137 °C and 226 °C), the reduction of dislocation density for both cases was quite similar. The difference of dislocation density between the EA annealing and IHT processes was insignificant, suggesting that the athermal effect of EA annealing was relatively small at those relatively low temperatures. Similar results were also reported on aluminum [11] and magnesium alloys [14,29]. The dislocation density of the IHT specimens only slightly decreased even when the peak

temperature was increased to 330 °C. In contrast, the dislocation density of the EA annealed specimens rapidly decreased as the peak temperature was increased from 226 to 330 °C, which suggests that the athermal effect of electric current became significant at the electric current density corresponding to the higher temperature. Among the five different annealing temperatures (or electric current densities), the dislocation densities of the EA annealed and IHT specimens showed the largest difference at the temperature of 330 °C. The dislocation density of  $4.39 \times 10^{13} \text{ m}^{-2}$  of the cold-rolled (as-received) specimen was reduced to  $4.33 \times 10^{12} \text{ m}^{-2}$  and  $1.48 \times 10^{13} \text{ m}^{-2}$  by EA annealing and IHT, respectively, at 330 °C. Therefore, the reduction of dislocation density by EA annealing ( $\Delta\rho = 3.96 \times 10^{13} \text{ m}^{-2}$ ) was approximately 36 % higher than by IHT ( $\Delta\rho = 2.91 \times 10^{13} \text{ m}^{-2}$ ) at 330 °C. The results of supplementary experiments with  $25 \text{ A/mm}^2$  (or at 275 °C) fit well with the trend of dislocation density reduction for both EA annealing and IHT. The difference in the dislocation density reduction diminished at the relatively high temperatures of 383 °C and 412 °C. However, the diminished difference in the results of EA annealing and IHT at the relatively high temperatures should be appreciated as a consequence of nearly complete annihilation of dislocation density. In fact, the contribution of athermal effect during EA annealing at the relatively high temperatures can still be observed in the microstructural change, as will be shown in the results of EBSD analysis.

Annealing through IHT occurs by thermal effect only, whereas EA annealing takes place by combined thermal and athermal effects. Therefore, it is believed that the difference between the dislocation densities of the EA annealed and IHT specimens in Fig. 2.5, except the results with nearly complete annihilation of dislocation, describe the athermal contribution of electric current in the dislocation density reduction during annealing. Comparison of the

dislocation density of the EA annealed and IHT specimens as a function of temperature suggests that the athermal contribution of electric current in the dislocation density reduction during the EA annealing process changes as the annealing temperature changes. Recently, Kim et al. [11] suggested the mechanism of electroplasticity in metals. In first principle calculation and experiments, they showed that the atomic bonding strength near defects can be additionally weakened by the athermal effect of electric current. This concept could explain the athermal contribution of electric current in EA annealing, as observed in our experiments. According to Kim et al. [11], the intensity of the athermal effect is quite low in low current density region (~low temperature region), which explains the insignificant difference between the effects of EA annealing and IHT at relatively low temperatures.

The results of microstructural observations by EBSD show that the as-received specimen had a microstructure comprised of deformed grains with an average grain size of  $10.8 \pm 9.7 \mu\text{m}$  (Figs. 2.6 and 2.7). After EA annealing (Fig. 2.6), a set of strain-free and



**Fig. 2.8.** Hardness of cold-rolled, EA annealed, and IHT specimens at different temperatures

equiaxed grains with low dislocation densities formed with full recrystallization, even at 383 °C (Fig. 2.6(e)), and a homogeneous grain growth state was achieved at 412 °C (Fig. 2.6(f)). However, the recrystallization and grain growth only partially occurred in IHT, even at the highest temperature of 412 °C (Fig. 2.7(f)). This confirms that athermal effect of electric current still exists at the temperatures of 383 °C and 412 °C. This finding also suggests that the athermal effect during EA annealing enhanced the rate of recrystallization [13,30] and grain growth during the process, in addition to the reduction of dislocation density, as presented above. As expected from the results of the dislocation density calculation and microstructural observation, the hardness of the EA annealed specimens (measured at the center of the top surface) was consistently lower than that of IHT specimens (Fig. 2.8), and the trend of hardness change corresponds well with that of the dislocation density calculation in Fig. 2.5.



## 2.4 CONCLUSIONS

The athermal contribution of electric current during EA annealing was assessed by comparing the performances of EA annealing and IHT. The calculation of reduction of dislocation density based on XRD measurement and the results of microstructural observation consistently suggest that EA annealing using the thermal effect of resistance heating and the athermal effect of electric current density can be more effective (energy-saving and cost-effective) compared to the conventional annealing process. However, as shown in the calculation of reduction of dislocation density and confirmed in the microhardness measurement, the additional effectiveness of EA annealing can be beneficial in a certain temperature range. At a relatively low temperature (or a low electric current density), EA annealing and IHT show nearly identical performance. Also, at an excessively high temperature, the thermal effect alone is able to induce nearly complete annihilation of dislocation density, thus, the practical advantage of EA annealing may diminish. Therefore, while EA annealing can be a very effective alternative to the conventional time-consuming annealing process with a furnace, in the design of EA annealing, electric current parameters and annealing temperature need to be carefully selected to properly benefit from the athermal contribution of electric current.

## REFERENCES FOR CHAPTER II

- [1] Nguyen-Tran, H.-D., Oh, H.-S., Hong, S.-T., Han, H. N., Cao, J., Ahn, S.-H., Chun, D.-M. (2015). A review of electrically-assisted manufacturing. *International Journal of Precision Engineering and Manufacturing-Green Technology*, 2, 365-376. <https://doi.org/10.1007/s40684-015-0045-4>
- [2] Ng, M.-K., Fan, Z., Gao, R. X., Smith, E. F., Cao, J. (2014). Characterization of electrically-assisted micro-rolling for surface texturing using embedded sensor. *CIRP Annals*, 63(1), 269-272. <https://doi.org/10.1016/j.cirp.2014.03.021>
- [3] Ng, M.-K., Li, L., Fan, Z., Gao, R. X., Smith, E. F., Ehmann, K. F., Cao, J. (2015). Joining sheet metals by electrically-assisted roll bonding. *CIRP Annals*, 64(1), 273-276. <https://doi.org/10.1016/j.cirp.2015.04.131>
- [4] Oh, H.-S., Cho, H.-R., Park, H., Hong, S.-T., Chun, D.-M. (2016). Study of electrically-assisted indentation for surface texturing. *International Journal of Precision Engineering and Manufacturing-Green Technology*, 3, 161-5. <https://doi.org/10.1007/s40684-016-0020-8>
- [5] Thien, N. T., Jeong, Y.-H., Hong, S.-T., Kim, M.-J., Han, H. N., Lee, M.-G. (2016). Electrically assisted tensile behavior of complex phase ultra-high strength steel. *International Journal of Precision Engineering and Manufacturing-Green Technology*, 3, 325-33. <https://doi.org/10.1007/s40684-016-0041-3>
- [6] Hong, S.-T., Li, Y.-F., Park, J.-W., Han, H. N. (2018). Effectiveness of electrically assisted solid-state pressure joining using an additive manufactured porous interlayer. *CIRP Annals*, 67(1), 297-300. <https://doi.org/10.1016/j.cirp.2018.04.062>

- [7] Li, Y.-F., Das, H., Hong, S.-T., Park, J.-W., Han, H. N. (2018). Electrically assisted pressure joining of titanium alloys. *Journal of Manufacturing Processes*, 35, 681-686. <https://doi.org/10.1016/j.jmapro.2018.09.015>
- [8] Luu, V. T., Dinh, T. K. A., Das, H., Kim, J.-R., Hong, S.-T., Sung, H.-M., Han, H. N. (2018). Diffusion Enhancement during Electrically Assisted Brazing of Ferritic Stainless Steel Alloys. *International Journal of Precision Engineering and Manufacturing-Green Technology*, 5, 613-621. <https://doi.org/10.1007/s40684-018-0063-0>
- [9] Jeong, H.-J., Park, J.-W., Jeong, K. J., Hwang, N. M., Hong, S.-T., Han, H. N. (2019). Effect of Pulsed Electric Current on TRIP-Aided Steel. *International Journal of Precision Engineering and Manufacturing-Green Technology*, 6, 315-27. <https://doi.org/10.1007/s40684-019-00060-1>
- [10] Dinh, K.-A., Hong, S.-T., Choi, S.-J., Kim, M.-J., Han, H. N. (2020). The Effect of Pre-strain and Subsequent Electrically Assisted Annealing on the Mechanical Behaviors of Two Different Aluminum Alloys. *International Journal of Precision Engineering and Manufacturing*, 21, 2345-2358. <https://doi.org/10.1007/s12541-020-00424-7>
- [11] Kim, M.-J., Yoon, S., Park, S., Jeong, H.-J., Park, J.-W., Kim, K., Jo, J., Heo, T., Hong, S.-T., Cho, S. H., Kwon, Y.-K., Choi, I.-S., Kim, M., Han, H. N. (2020). Elucidating the origin of electroplasticity in metallic materials. *Applied Materials Today*, 21. <https://doi.org/10.1016/j.apmt.2020.100874>
- [12] Kim, M.-J., Lee, K., Oh, K. H., Choi, I.-S., Yu, H.-H., Hong, S.-T., Han, H. N. (2014). Electric current-induced annealing during uniaxial tension of aluminum alloy. *Scripta Materialia*, 75, 58-61. <https://doi.org/10.1016/j.scriptamat.2013.11.019>

- [13] Park, G. D., Tran, V. L., Hong, S.-T., Jeong, Y.-H., Yeo, T. S., Nam, M. J., Kim, M.-J., Jin, S.-W., Han, H. N. (2017). Electrically assisted stress relief annealing of automotive springs. *Journal of Mechanical Science and Technology*, 31, 3943-3948. <https://doi.org/10.1007/s12206-017-0740-x>
- [14] Liu, K., Dong, X.-H., Shi, W. (2019). Effect of pulsed current on AZ31B magnesium sheets during annealing. *Transactions of Nonferrous Metals Society of China*, 29(4), 735-740. [https://doi.org/10.1016/S1003-6326\(19\)64983-6](https://doi.org/10.1016/S1003-6326(19)64983-6)
- [15] Guan, L., Tang, G., Chu, P. K. (2011). Recent advances and challenges in electroplastic manufacturing processing of metals. *Journal of Materials Research*, 25(7), 1215-1224. <https://doi.org/10.1557/JMR.2010.0170>
- [16] Conrad, H. (2000). Electroplasticity in metals and ceramics. *Materials Science and Engineering: A*, 287(2), 276-87. [https://doi.org/10.1016/S0921-5093\(00\)00786-3](https://doi.org/10.1016/S0921-5093(00)00786-3)
- [17] Magargee, J., Morestin, F., Cao, J. (2013). Characterization of Flow Stress for Commercially Pure Titanium Subjected to Electrically-Assisted Deformation. *Journal of Engineering Materials and Technology*, 135(4), 041003. <https://doi.org/10.1115/1.4024394>
- [18] Roh, J.-H., Seo, J.-J., Hong, S.-T., Kim, M.-J., Han, H. N., Roth, J. T. (2014). The mechanical behavior of 5052-H32 aluminum alloys under a pulsed electric current. *International Journal of Plasticity*, 58, 84-99. <https://doi.org/10.1016/j.ijplas.2014.02.002>
- [19] Hariharan, K., Lee, M.-G., Kim, M.-J., Han, H. N., Kim, D., Choi, S. (2015). Decoupling Thermal and Electrical Effect in an Electrically Assisted Uniaxial Tensile Test Using Finite Element Analysis. *Metallurgical and Materials Transactions A*, 46, 3043-3051. <https://doi.org/10.1007/s11661-015-2879-3>

- [20] Ghiotti, A., Bruschi, S., Simonetto, E., Gennari, C., Calliari, I., Bariani, P. (2018). Electroplastic effect on AA1050 aluminium alloy formability. *CIRP Annals*, 67(1), 289-292. <https://doi.org/10.1016/j.cirp.2018.04.054>
- [21] Park, S., Kim, D.-W., Kim, J.-H., Lee, S. Y., Kwon, D., Han, H. N. (2020). A Finite Element Simulation for Induction Heat Treatment of Automotive Drive Shaft. *ISIJ International*, 60 (6), 1333-1341. <https://doi.org/10.2355/isijinternational.ISIJINT-2019-466>
- [22] Enzo, S., Fagherazzi, G., Benedetti, A., Polizzi, S. (1988). A profile-fitting procedure for analysis of broadened X-ray diffraction peaks. I. Methodology. *Journal of Applied Crystallography*, 21, 536-542. <https://doi.org/10.1107/S0021889888006612>
- [23] Ida, T., Ando, M., Toraya, H. (2000). Extended pseudo-Voigt function for approximating the Voigt profile. *Journal of Applied Crystallography*, 33, 1311-1316. <https://doi.org/10.1107/S0021889800010219>
- [24] Williamson, G. K., Hall, W. H. (1953). X-ray line broadening from filed aluminium and wolfram. *Acta Metallurgica*, 1(1), 22-31. [https://doi.org/10.1016/0001-6160\(53\)90006-6](https://doi.org/10.1016/0001-6160(53)90006-6)
- [25] Ungár, T. (2004). Microstructural parameters from X-ray diffraction peak broadening. *Scripta Materialia*, 51(8), 777-781. <https://doi.org/10.1016/j.scriptamat.2004.05.007>
- [26] Ungár, T., Ott, S., Sanders, P. G., Borbély, A., Weertman, J. R. (1998). Dislocations, grain size and planar faults in nanostructured copper determined by high resolution X-ray diffraction and a new procedure of peak profile analysis. *Acta Materialia*, 46(10), 3693-3699. [https://doi.org/10.1016/S1359-6454\(98\)00001-9](https://doi.org/10.1016/S1359-6454(98)00001-9)
- [27] Oh, Y., Kwak, N., Lee, K., Ko, W.-S., Han, H. N. (2019). Ductility enhancement of tungsten after plastic deformation. *Journal of Alloys and Compounds*, 787, 801-814. <https://doi.org/10.1016/j.jallcom.2019.02.097>

- [28] Williamson, G. K., Smallman, R. E. (1956). III. Dislocation densities in some annealed and cold-worked metals from measurements on the X-ray debye-scherrer spectrum. *Philosophical Magazine*, 1(1), 34-46. <https://doi.org/10.1080/14786435608238074>
- [29] Liu, K., Dong, X., Xie, H., Peng, F. (2015). Effect of pulsed current on the deformation behavior of AZ31B magnesium alloy. *Materials Science and Engineering: A*, 623, 97-103. <https://doi.org/10.1016/j.msea.2014.11.039>
- [30] Park, J.-W., Jeong, H.-J., Jin, S.-W., Kim, M.-J., Lee, K., Kim, J. J., Hong, S.-T., Han, H. N. (2017). Effect of electric current on recrystallization kinetics in interstitial free steel and AZ31 magnesium alloy. *Materials Characterization*, 133, 70-76. <https://doi.org/10.1016/j.matchar.2017.09.021>
- [31] Jeong, H.-J., Kim, M.-J., Choi, S.-J., Park, J.-W., Choi, H., Luu, V. T., Hong, S.-T., Han, H. N. (2020). Microstructure reset-based self-healing method using sub-second electric pulsing for metallic materials. *Applied Materials Today*, 20. <https://doi.org/10.1016/j.apmt.2020.100755>

## CHAPTER III

# ELECTRICALLY ASSISTED SOLID-STATE JOINING OF CrMnFeCoNi HIGH-ENTROPY ALLOY

### ABSTRACT

Equiatomic CrMnFeCoNi high-entropy alloy was joined in solid-state by electrically assisted pressure joining (EAPJ). Cracks and compositional segregation were not found in joining zones (JZ). As the applied electric current increased, the microstructure of JZ changed from a deformed and partially recrystallized microstructure to a fully recrystallized one with grain growth. JZ showed sound mechanical properties through the Vickers hardness and uniaxial tension results. EAPJ of high-entropy alloy can overcome the disadvantage of fusion welding.

**Keywords:** High-entropy alloys; Electrically assisted pressure joining; Electroplasticity; Finite element modeling; Recrystallization

### 3.1 INTRODUCTION

Since defining and classifying alloys as configurational entropy terms began in 2004, numerous studies have been reported on high-entropy alloys (HEAs) [1,2]. HEA, which has a concept of composing elements different from conventional alloys, has excellent material properties and shows potential as a structural material. Gludovatz et al. [3] reported that equiatomic CrMnFeCoNi HEA had excellent fracture toughness due to twinning-induced plasticity behavior at cryogenic temperatures. Li et al. [4] overcame the strength-ductility trade-off phenomenon using metastability of transformation-induced plasticity-assisted dual phase HEA. Several HEAs also showed excellent physical properties when exposed to specific environments. A face-centered cubic (FCC) type HEA showed excellent hydrogen embrittlement resistance after hydrogen-charging in the gaseous state [5,6]. Besides, a body-centered cubic (BCC) type HEA composed of refractory elements showed excellent high temperature mechanical properties [7]. Furthermore, by intentionally forming a second phase [8,9] or a precipitate such as a carbide or Ni<sub>3</sub>Al gamma prime [10,11], the mechanical properties of HEAs were improved.

Numerous studies on the weldability of HEAs have been conducted, and they show great potential as structural materials. The weldability of various HEAs has been evaluated using friction stir welding (FSW) [12], fusion welding using an electron beam welding [13], laser welding [14], and gas tungsten arc welding [15]. In addition, the welding [16] or brazing [17] of HEAs with dissimilar materials have been reported. The above-mentioned studies have shown that HEAs have good weldability. However, fusion welding results in a dendritic structure as well as chemical inhomogeneity of the high-entropy composition [14,15]. This is



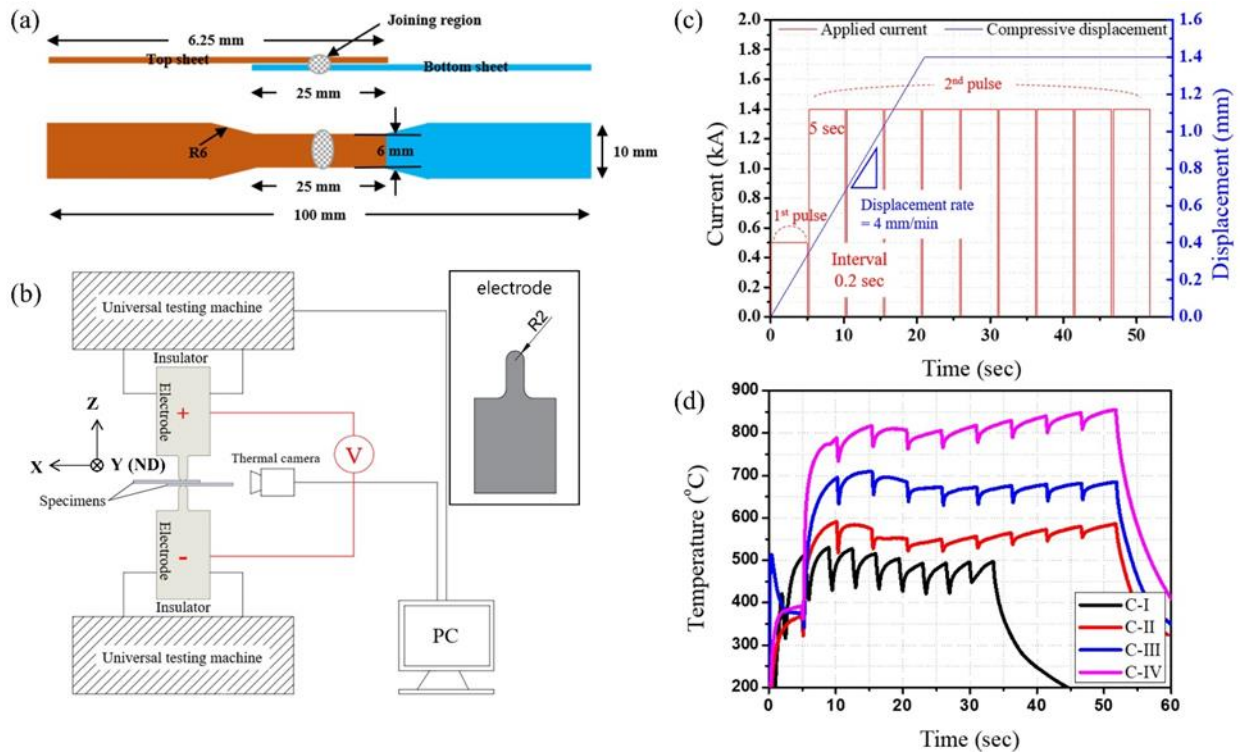
inevitable not only in FCC HEAs but also in refractory BCC HEAs [2,7]. Due to the phase instability of HEAs at intermediate temperatures [18], the chemical segregation can promote phase decomposition. Additionally, fusion welding may cause solidification cracking due to various reasons [19].

Solid-state joining can be utilized to overcome the disadvantages of fusion welding of HEAs. It has been shown that FSW can be an effective solid-state joining technique for HEAs [12,14]. However, FSW requires specific facilities, expensive tools, and has a limited joint geometry. Therefore, in this study, as a solid-state joining technique of HEAs, we proposed electrically assisted pressure joining (EAPJ), which can be completed in solid-state within a relatively very short time by simultaneously applying electric current and plastic compressive deformation. The concept of EAPJ is based on kinetic enhancement due to the athermal effect of applied electric current, which is distinct from the thermal effect due to Joule heating [20-23]. The results of successful solid-state joining by EAPJ have been reported for various conventional alloys, such as 316 stainless steel, Cu-Zn alloy, and Ti alloy [24,25]. In the present work, we investigate the feasibility of EAPJ of CrMnFeCoNi HEA to produce a sound solid-state joint at a temperature substantially lower than its melting point, and the effect of an applied electric current pattern on the microstructural change in Joining Zones (JZs).

### 3.2 EXPERIMENTAL SET-UP

An ingot having equiatomic ratio of Cr, Mn, Fe, Co, and Ni was fabricated by vacuum induction melting. Hot rolling at about 1100 °C was performed to reduce the thickness of the ingot from 85 mm to 21 mm. For chemical homogenization, heat treatment was performed at 1200 °C for 48 hours followed by water cooling. After the homogenization treatment, to remove the grain growth during heat treatment, cold rolling was conducted to reduce the thickness of plate to 3.5 mm (reduction of about 83%). A recrystallization heat treatment was then conducted at 1000 °C for 1 hour followed by water cooling. Next, the recrystallized 3.5 mm thick HEA plate was cut to a half-thickness (1.75 mm) along the direction perpendicular to the thickness direction. Wire cutting was then performed to prepare half of the sub-size ASTM-E8M tensile specimen, as shown in Fig. 3.1(a). Finally, the surface of specimen was polished using 100-grit SiC sandpaper to remove the oxide layer and oil.

A custom-made fixture for EAPJ was installed in a universal testing machine and connected with a programmable electric power supply, as illustrated in Fig. 3.1(b). Bakelite insulators were used to isolate the universal testing machine from the electric circuit. Punches with a 2 mm radius tip, which also worked as electrodes, were made using tool steel (inset of Fig. 3.1(b)). A pre-force of 200 N was applied to the specimen assembly before an electric current was applied to ensure good contact between dies and the specimen. The temperature of specimen was measured by an infrared thermal imaging camera (FLIR-T621, FLIR, Sweden). One side (transverse side) of the sample was painted with a thin layer of heat-resistant black paint to stabilize the emissivity.



**Fig. 3.1.** (a) Geometry of specimen for tensile-shear tests for EAPJ, (b) schematic of the experimental set-up for EAPJ, (c) experimental conditions for applied current and compressive displacement, and (d) measured temperature history during EAPJ

For EAPJ, the electric current and compressive displacement with a constant crosshead speed of 4 mm/min were simultaneously applied to the specimen assembly after reaching the preset pre-load, as shown in Fig. 3.1(c). The experiment was carried out using four different patterns (C-I, C-II, C-III, and C-IV) of electric current, as listed in Table 3.1. For all current patterns, a compressive displacement of 1.4 mm (~70 % reduction) was applied and maintained at this final value before the completion of electric current. During the EAPJ, the temperature history reached a near-plateau with serration, especially during the 2<sup>nd</sup> pulse, as shown in Fig. 3.1(d). As expected, with a different current pattern, the temperature history showed a different plateau value and a different average joining temperature, which could be

**Table 3.1. The electric current conditions for EAPJ**

Electric current pattern	1 <sup>st</sup> pulse		2 <sup>nd</sup> pulse			Cycle	Total time (sec)
	Current (kA)	Duration (sec)	Current (kA)	Duration (sec)	Interval (sec)		
C-I	0.2	2	0.5	3	0.5	9	33.5
C-II	0.5	5	1.0	5	0.2	9	51.8
C-III	0.5	5	1.2	5	0.2	9	51.8
C-IV	0.5	5	1.4	5	0.2	9	51.8

obtained as the average of peak temperatures in the plateau. To confirm the repeatability of the results, the experiment for each condition was repeated at least three times.

Microstructure observations and mechanical properties measurements were performed to confirm a successful solid-state joining. Microstructure observations were performed mainly at the joint cross-section (transverse direction, Y direction in Fig. 3.2(a)) using a scanning electron microscope (SEM) (S-4300SE, Hitachi, Japan) equipped with electron backscatter diffraction (EBSD) (e-Flash, Bruker, USA) and energy dispersive spectrometry (EDS) (XFlash detector 5030, Bruker, USA). For EBSD analysis, the cross-section of the specimen was electropolished with a Struers A2 solution and analyzed with commercial software (TSL OIM Analysis 7.3.0, EDAX, USA). Mechanical properties were evaluated on the transverse side of the joint using a micro Vickers hardness machine (HM-122, Mitutoyo, Japan) with a 4.9 N (500 gf) load and a duration of 10 sec at an interval of 500  $\mu\text{m}$ . A uniaxial tension test was also performed to evaluate the soundness of the EAPJ joint with a crosshead speed of 1 mm/min.

An inverse finite element simulation of uniaxial tensile test was conducted through the continuum-based finite element method (FEM) using an elasto-plastic constitutive model to investigate the mechanical properties of JZ for the C-I and C-IV conditions and compared with the non-joined base metal (C-O). For the finite element simulation, the sub-size tensile specimen was simply divided into two solid sections: JZ and base metal (BM) as shown in supplementary Fig. 3.6. The pressed region by the punch was indented slightly inward in the thickness direction. The dimensions of the JZ for each condition are also shown in supplementary Fig. 3.6. The 3 dimensional 8-node continuum elements (C3D8) were used with the total number of elements, 28272 (C-I) and 27370 (C-IV), respectively. The von Mises yield function and isotropic hardening model were used for the simulation of uniaxial tension for joined HEA. The stress-strain curve of investigated HEA was optimized with the Swift hardening equation as follows:

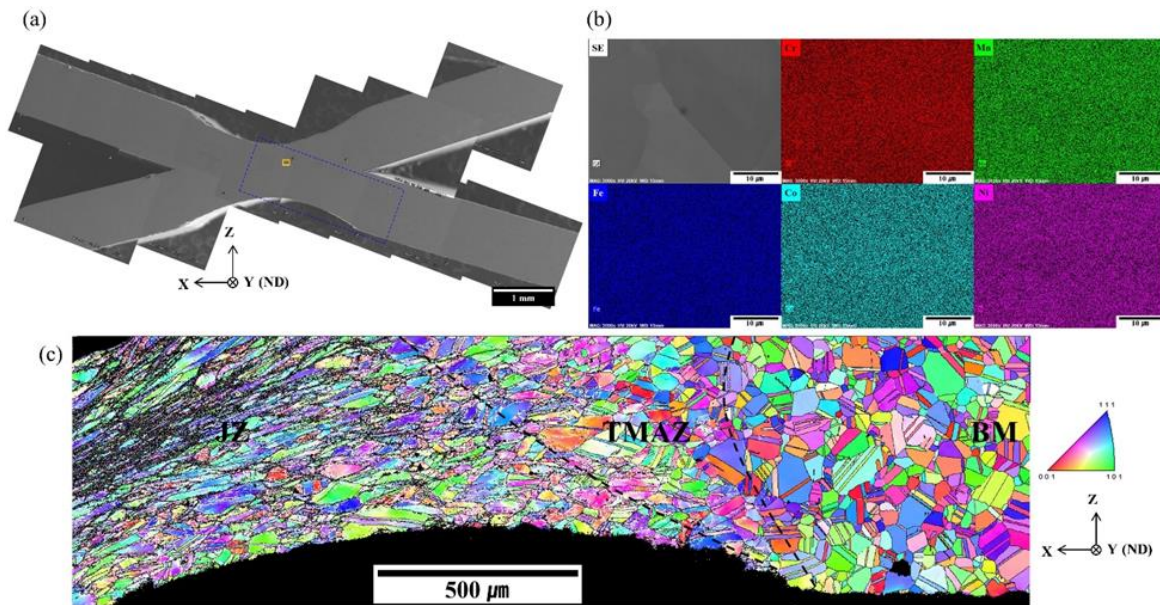
$$\sigma = K(\varepsilon_0 + \bar{\varepsilon}_p)^n \quad (1)$$

where  $K$ ,  $\varepsilon_0$ , and  $n$  are material constants. The material constants for non-joined base metal (C-O) were obtained from the measured stress-strain curve and those for JZ were inversely optimized from the experimentally measured load–displacement curve for C-I and C-IV specimens. The objective function of Eq. (2) was obtained based on the discrepancy in flow stress data between the experiments and numerical simulations and a new set of materials parameters were generated during the optimization process. The FE simulation was repeated until an optimum set of parameters which minimized the objective function.

$$\sum_{i=1}^n \left( \sigma_{\text{experimental}}^i - \sigma_{\text{simulated}}^i \right) = \text{min.} \quad (2)$$

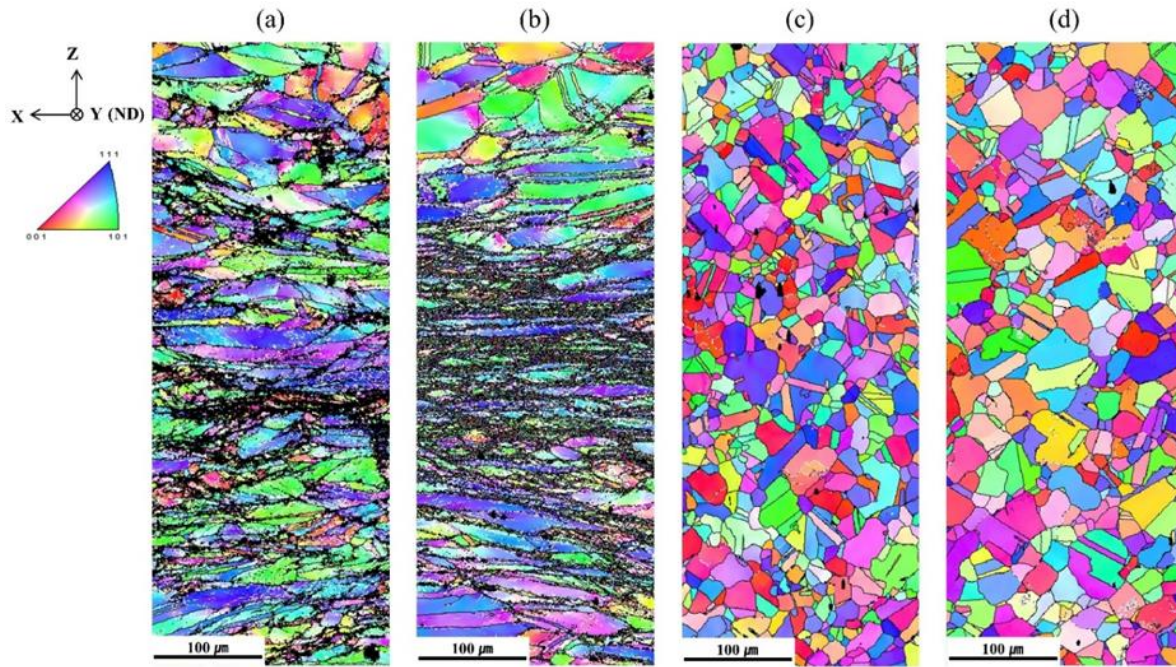
### 3.3 RESULTS AND DISCUSSIONS

Figure 3.2(a) represents a transverse direction SEM micrograph of the joined specimen with C-I current pattern. Round indentations were observed on the top and bottom surfaces due to the compression during joining. As shown in Fig. 3.2(a), no specific macro- and micro-crack was observed in this specimen even under this joining condition with the lowest average joining temperature of 508 °C. SEM-EDS analysis of the joint center (yellow box in Fig. 3.2(a)) under high magnification (x3000) showed no macro- and micro-compositional segregation with C-IV current pattern (Fig. 3.2(b)). In C-IV current pattern, the average joining temperature was 824 °C, which was the highest temperature in this work.



**Fig. 3.2.** (a) Typical cross-section of EAPJ collage. (b) high magnification (x3000) SEM-EDS element maps (Cr, Mn, Fe, Co, and Ni) of joining center with C-IV current pattern (yellow box region in Fig. 3.2(a)) and ND IPF map from JZ to BM with C-II current pattern (marked as a blue rectangle in Fig. 3.2(a))

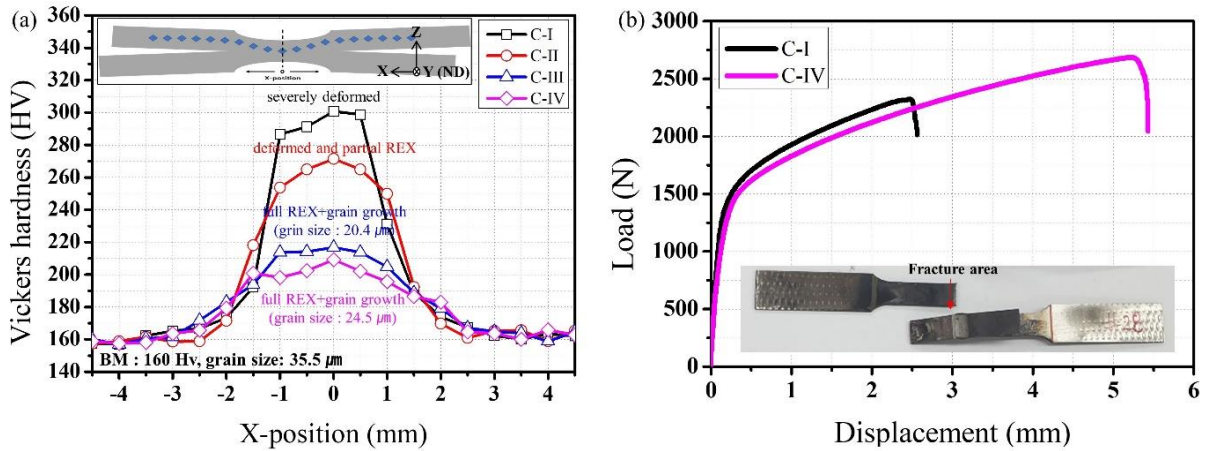
The other current conditions also showed the same results as those for C-IV. It was confirmed that at about only 40% of the melting temperature (C-I), a macro- and micro-defect-free solid-state joint was formed by EAPJ. This may be understood to be the result of enhanced diffusion by a combination of Joule heating and the athermal effect of the electric current [20–23]. Figure. 3.2(c) shows EBSD inverse pole figure (IPF) maps taken from the region indicated by the blue rectangle in Fig. 3.2(a) under C-II pattern with an average joining temperature of 571 °C. The orientation map illustrates the significant microstructural change from the joint center to the BM. Kernel average misorientation (KAM) map shown in supplementary Fig. 3.7 provides information regarding the deformed microstructure. According to these microstructural changes, the joining materials can be classified into the JZ, thermo-mechanically affected zone (TMAZ), and BM. In C-II pattern, we observed both deformed and partially recrystallized grain structures in the JZ. The parent grains in the TMAZ did not show significant growth. It can be concluded that the increase in temperature during EAPJ in C-II is not sufficient for grain growth in the TMAZ.



**Fig. 3.3.** ND IPF maps of JZ centers: (a) C-I, (b) C-II, (c) C-III, and (d) C-IV

IPF maps of the JZ under each joining condition were analyzed as shown in Fig. 3.3. It can be seen that the grains were considerably deformed at the joint center along the perpendicular to the compression loading direction as shown in Figs. 3.3(a and b). As mentioned above, Fig. 3.3(b) shows that partial recrystallization (REX) occurred in the joint center under C-II condition. The increase of average joining temperature to approximately 685 °C (C-III pattern) resulted in full REX and grain growth as shown in Fig. 3.3(c). It should be noted that under C-III pattern, full REX and grain growth occurred at a much lower temperature than the static REX temperature of CrMnFeCoNi HEA, which was reported to be 800~900 °C [26]. Also, under C-III condition, unlike C-II, we obtained a homogeneous microstructure throughout the JZ after REX and grain growth ( $20.4 \pm 9.3 \mu\text{m}$ ) as shown in IPF map (see supplementary Fig. 3.8). In C-IV condition (Fig. 3.3(d)), the average joining temperature increased to 824 °C and a larger grain size ( $24.5 \pm 10.1 \mu\text{m}$ ) in the JZ, which is





**Fig. 3.4.** (a) Vickers hardness profile at 500 μm intervals in cross-section of EAPJ joint along with the blue dots in the inset and (b) tensile-shear test results of the non-REX (C-I) and full REX (C-IV) EAPJ specimens

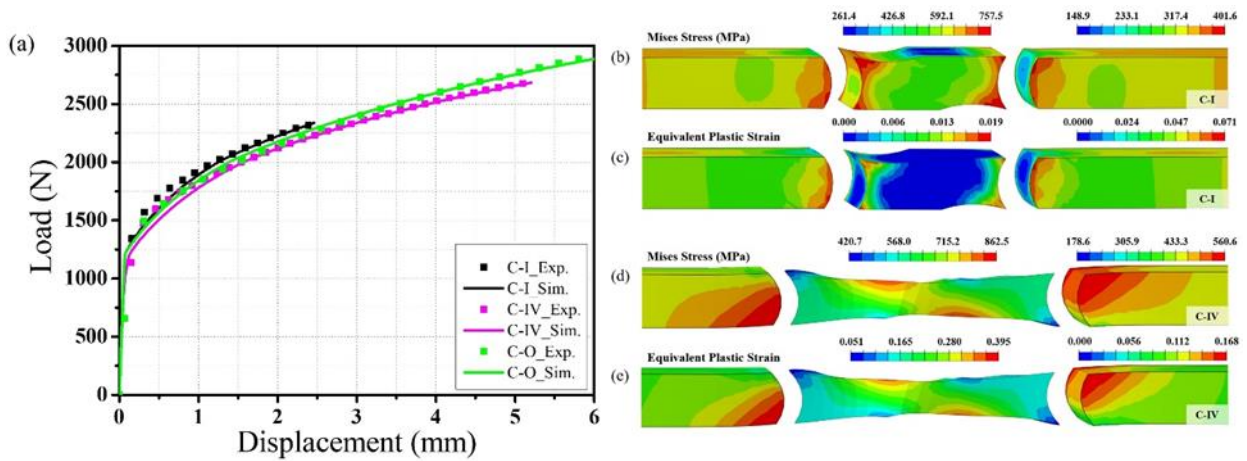
slightly smaller than that in the BM ( $35.5 \pm 16.4 \mu\text{m}$ ), was obtained.

The distributions of micro-hardness in EAPJ joints were measured (Fig. 3.4(a)). For all current patterns, the hardness increased significantly in the joint center than BM (160 Hv). As indicated in Fig. 3.4(a), different microstructures were developed according to the applied current patterns, and the measured hardness distributions agreed well with the resultant microstructures. Figure 3.4(b) shows the uniaxial tension test results of non-REX (C-I) and full REX (C-IV) specimens. For all joining conditions, the EAPJ specimens failed at the BM near the joint area. The mechanical properties of JZ for the joined specimens were investigated from inverse FE simulation for uniaxial tensile test. The parameters of Swift law for BM were obtained from the measured stress strain curve and the resulting parameters are listed in Table. 3.2. The load displacement curves for the joined specimens were used to optimize the Swift parameters for JZ. Figure 3.5(a) shows the experimental and simulated load displacement curves.

The mechanical properties of JZ for the joined specimens were investigated from inverse FE simulation for uniaxial tensile test. The parameters of Swift law for BM were obtained from the measured stress strain curve and the resulting parameters are listed in Table. 3.2. The load-displacement curves for the joined specimens were used to optimize the Swift parameters for JZ. Figure 3.5(a) shows the experimental and simulated load-displacement curves using optimized parameters, which is listed in Table. 3.2. In the case of C-I condition, since the JZ has undergone plastic deformation during the joining process (Fig. 3.4(a)), the hardening exponent is lower than that of the C-IV condition. The yield stresses for each case are 180.7 MPa for C-O, 578.1 MPa for C-I, and 214.78 MPa for C-IV, respectively, which agree well with the tendency of hardness and grain size measured experimentally.

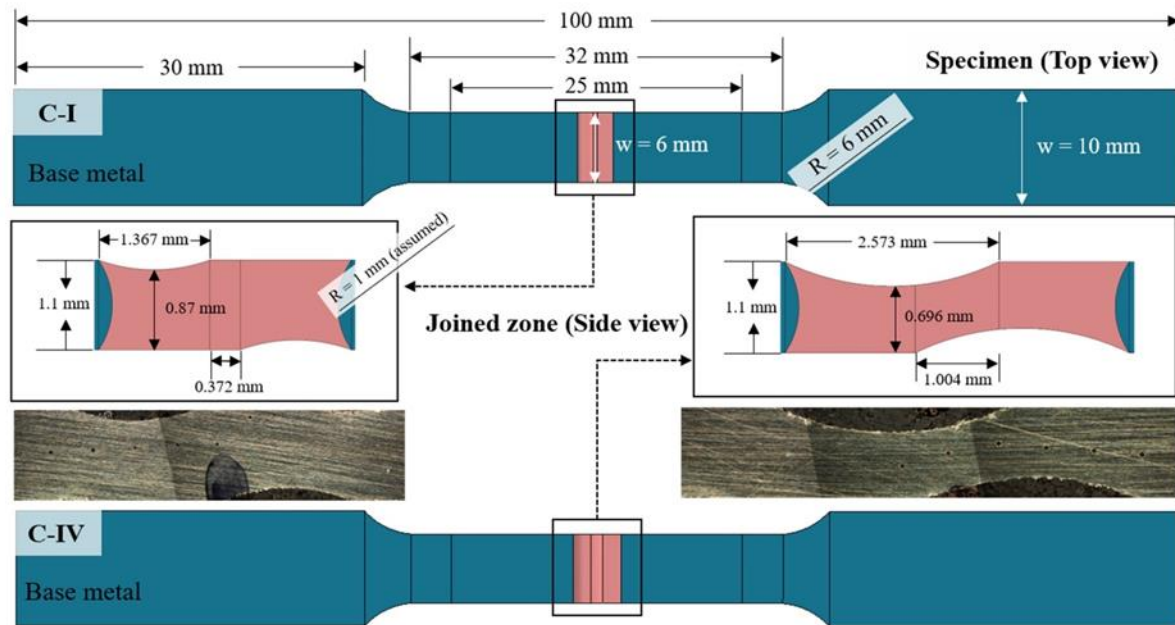
**Table 3.2. The material parameters of Swift equation for BM and JZ**

	A	$\epsilon_0$	n
BM	1186	0.01377	0.4391
JZ (C-I)	1917	0.01568	0.2885
JZ (C-IV)	1261	0.01587	0.4272

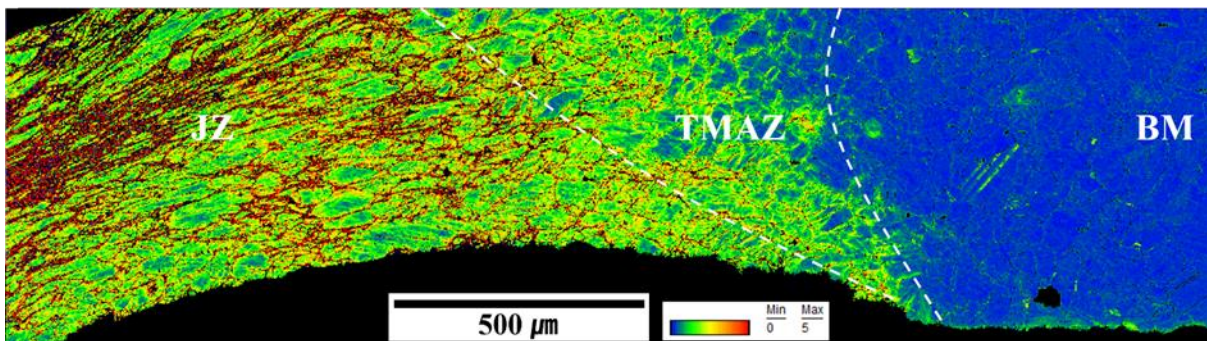


**Fig. 3.5.** (a) The experimental and simulated load-displacement curves of the non-REX (C-I), full REX (C-IV) EAPJ specimens and non-joined base metal (C-O) using optimized parameters and the contour maps of von Mises stress (b, d) and equivalent plastic strain (c, e) for JZ and BM of EAPJ specimens at the onset of fracture

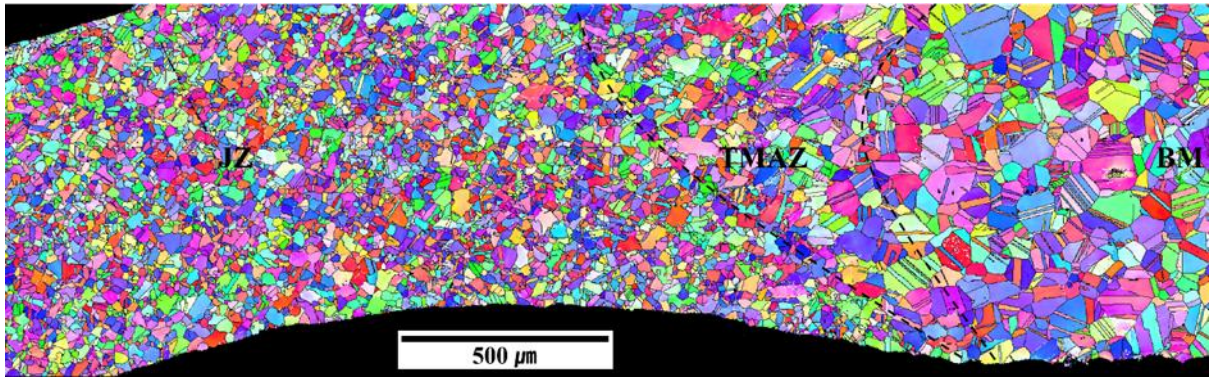
Figure 3.5(b) presents the contour maps of von Mises stress and equivalent plastic strain for JZ and BM at the onset of fracture. As mentioned above, since the JZ is compressed by a punch, it was observed that the deformation was concentrated during uniaxial tension. The maximum values of von Mises stress and equivalent plastic strain for C-I are 757.5 MPa and 0.071, respectively, whereas 862.5 MPa and 0.395 for C-IV. Considering that the maximum von Mises stress and equivalent plastic strain of the gage section in non-joined base metal (C-O) at the onset of fracture are 744.6 MPa and 0.333, respectively, the maximum von Mises stress in both EAPJ conditions is higher than that of non-joined base metal.



**Fig. 3.6.** (Supplementary Figure) Finite element models of the uniaxial tensile test for C-I and C-IV



**Fig. 3.7.** (Supplementary Figure) KAM map from JZ to BM with C-II current pattern. (marked as a blue rectangle in Fig. 2(a))



**Fig. 3.8.** (Supplementary Figure) ND IPF map from JZ to BM with C-III current pattern

### **3.4 CONCLUSION**

EAPJ was performed by applying plastic compressive deformation and electric current on CrMnFeCoNi HEA sheets. In a remarkably short time, a solid-state joint was successfully made without macro- and micro-cracks and compositional segregation. With the increase of electric current, the JZ changed from a deformed and partially recrystallized microstructure to a fully recrystallized one with grain growth. The mechanical properties of the JZ were investigated through uniaxial tensile tests and inverse finite element methods, and the obtained mechanical properties showed good agreement with the tendency of the experimentally measured hardness values. The HEA joined by EAPJ showed sound mechanical properties. It was confirmed that the EAPJ can overcome the disadvantages of fusion welding for HEA.

## **ACKNOWLEDGEMENT**

This work was supported by National Research Foundation of Korea (NRF) grants funded by Korea government (MSIT) (2018R1A2B6006856, 2019R1A2C2009939, 2020R1A5A6017701, and 2019M3D1A1079215). The Institute of Engineering Research at Seoul National University provided research facilities for this work.

## REFERENCES FOR CHAPTER III

- [1] J.W. Yeh, S.K. Chen, S.J. Lin, J.Y. Gan, T.S. Chin, T.T. Shun, C.H. Tsau, and S.Y. Chang: *Adv. Eng. Mater.*, 2004, vol. 6, pp. 299–303.
- [2] B. Cantor, I.T.H. Chang, P. Knight, and A.J.B. Vincent: *Mater. Sci. Eng. A*, 2004, vols. 375–377, pp. 213–18.
- [3] B. Gludovatz, A. Hohenwarter, D. Catoor, E.H. Chang, E.P. George, and R.O. Ritchie: *Science*, 2014, vol. 345, pp. 1153–58.
- [4] Z. Li, K.G. Pradeep, Y. Deng, D. Raabe, and C.C. Tasan: *Nature*, 2016, vol. 534, pp. 227–30.
- [5] Y. Zhao, D.H. Lee, M.Y. Seok, J.A. Lee, M.P. Phaniraj, J.Y. Suh, H.Y. Ha, J.Y. Kim, U. Ramamurty, and J. Il Jang: *Scr. Mater.*, 2017, vol. 135, pp. 54–58.
- [6] Z. Pu, Y. Chen, and L.H. Dai: *Mater. Sci. Eng. A*, 2018, vol. 736, pp. 156–66.
- [7] O.N. Senkov, G.B. Wilks, J.M. Scott, and D.B. Miracle: *Intermetallics*, 2011, vol. 19, pp. 698–706.
- [8] D. Choudhuri, S. Shukla, P.A. Jannotti, S. Muskeri, S. Mukherjee, J.T. Lloyd, and R.S. Mishra: *Mater. Charact.*, 2019, vol. 158, p. 109955.
- [9] L.A. Santos, S. Singh, and A.D. Rollett: *Metall. Mater. Trans. A Phys. Metall. Mater. Sci.*, 2019, vol. 50, pp. 5433–44.
- [10] H. Yang, J. Li, T. Guo, W.Y. Wang, H. Kou, and J. Wang: *Met. Mater. Int.*, 2019, vol. 25, pp. 1145–50.
- [11] X.W. Liu, L. Liu, G. Liu, X.X. Wu, D.H. Lu, J.Q. Yao, W.M. Jiang, Z.T. Fan, and W.B. Zhang: *Metall. Mater. Trans. A Phys. Metall. Mater. Sci.*, 2018, vol. 49, pp. 2151–60.



- [12] M. Komarasamy, N. Kumar, Z. Tang, R.S. Mishra, and P.K. Liaw: *Mater. Res. Lett.*, 2014, vol. 3, pp. 30–34.
- [13] Z. Wu, S.A. David, Z. Feng, and H. Bei: *Scr. Mater.*, 2016, vol. 124, pp. 81–85.
- [14] M.-G. Jo, H.-J. Kim, M. Kang, P.P. Madakashira, E.S. Park J.-Y. Suh, D.-I. Kim, S.-T. Hong, and H.N. Han: *Met. Mater. Int.*, 2018, vol. 24, pp. 73–83.
- [15] Z. Wu, S.A. David, D.N. Leonard, Z. Feng, and H. Bei: *Sci. Technol. Weld. Join.*, 2018, vol. 23, pp. 585–95.
- [16] R. Sokkalingam, V. Muthupandi, K. Sivaprasad, and K.G. Prashanth: *J. Mater. Res.*, 2019, pp. 2683–94.
- [17] C. Lin, R.K. Shiue, S.K. Wu, and Y.S. Lin: *Crystals*, 2019, vol. 9, pp. 1–17.
- [18] F. Otto, A. Dlouhy , K.G. Pradeep, M. Kubeř nova , D. Raabe, G. Eggeler, and E.P. George: *Acta Mater.*, 2016, vol. 112, pp. 40–52.
- [19] S. Kou: *Acta Mater.*, 2015, vol. 88, pp. 366–74.
- [20] H. Conrad: *Mater. Sci. Eng. A*, 2000, vol. 287, pp. 276–87.
- [21] J.H. Roh, J.J. Seo, S.T. Hong, M.J. Kim, H.N. Han, and J.T. Roth: *Int. J. Plast.*, 2014, vol. 58, pp. 84–99.
- [22] M.J. Kim, K. Lee, K.H. Oh, I.S. Choi, H.H. Yu, S.T. Hong, and H.N. Han: *Scr. Mater.*, 2014, vol. 75, pp. 58–61.
- [23] J.W. Park, H.J. Jeong, S.W. Jin, M.J. Kim, K. Lee, J.J. Kim, S.T. Hong, and H.N. Han: *Mater. Charact.*, 2017, vol. 133, pp. 70–76.
- [24] H.J. Jeong, M.J. Kim, S.J. Choi, J.W. Park, H. Choi, V.T. Luu, S.T. Hong, and H.N. Han: *Appl. Mater. Today*, 2020, vol. 20, p. 100755.

- [25] L. Peng, Z. Xu, and X. Lai: *Proc. Inst. Mech. Eng. Part B J. Eng. Manuf.*, 2014, vol. 228, pp. 582–94.
- [26] Y.F. Li, H. Das, S.T. Hong, J.W. Park, and H.N. Han: *J. Manuf. Process.*, 2018, vol. 35, pp. 681–86.
- [27] S.J. Sun, Y.Z. Tian, H.R. Lin, H.J. Yang, X.G. Dong, Y.H. Wang, and Z.F. Zhang: *Mater. Sci. Eng. A*, 2018, vol. 712, pp. 603–07.
- [28] Z. Wang, W. Lu, D. Raabe, and Z. Li: *J. Alloys Compd.*, 2019, vol. 781, pp. 734–43.
- [29] S.J. Marcadet and D. Mohr: *Int. J. Fract.*, 2016, vol. 200, pp. 77–98.
- [30] F. Otto, N.L. Hanold, and E.P. George: *Intermetallics*, 2014, vol. 54, pp. 39–48.

**CHAPTER IV**

**ELECTRICALLY ASSISTED PRESSURE JOINING OF ALUMINIUM  
CLAD ALUMINUM ALLOY**

**ABSTRACT**

The electrically assisted pressure joining (EAPJ) of thin bi-layer cold-rolled aluminum-clad aluminum (Al-clad Al) sheets, which are developed for the battery containers of electric vehicles, is experimentally investigated. A compressive displacement is applied to the specimen assembly in lap configuration to induce plastic deformation of the joining area while a pulsed electric current with varying current density is simultaneously applied through the joining area. Microstructure analysis shows that the thin Al-clad Al sheets are successfully joined in the solid-state at a temperature significantly lower than the melting temperatures of the selected alloys without damaging the integrity of the bi-layer sheets. The results indicate the presence of deformed, elongated grains and Si particles distributed from the clad to the core layers during joining. The mechanical properties of the joint are also evaluated through uniaxial tension and hardness measurements. The results of the present study suggest that the concept of EAPJ is applicable to the newly developed bi-layer sheets used for electric vehicle components.

**Keywords:** aluminum-clad aluminum; electrically assisted; solid-state joining

## 4.1 INTRODUCTION

Over the past few decades, weight reduction has become a significant concern for automobile industries, especially for Battery-Driven Electric Vehicles (BEVs). The battery case and its related components are bulkier and heavier than the corresponding components in fossil fuel-powered vehicles. In recent years, a wide selection of aluminum alloys has been used for lightweight structures in BEVs, enabling weight reduction of the battery-pack system [1,2]. Additionally, the battery packs of BEVs consist of thousands of cells that generate a large amount of heat under strong charging and discharging conditions. As a result, the battery cell temperature is significantly elevated by the high current cycles required for high performance and high charging rate [3]. However, the BEV battery life cycle is reduced when high battery temperatures persist for extended periods of time. Therefore, in addition to reducing the weight of the battery-pack system, it is essential to enhance the performance of its cooling system to extend the life span of the battery. Several different cooling methods, including immersion cooling, forced air systems, and cooling systems with a cooling plate or cooling liquid, have been suggested for controlling the working temperature BEV batteries. However, only considering cooling techniques without regard for their weight will not meet the demand for a light and high-performance BEV battery system.

For cost-effective and lightweight structures for the battery system, the application of multilayer clad sheets can be considered. The combined properties of the core and skin of bi/multilayer clad sheets enhance the properties of the candidate material compared to the individual materials or alloys for focused applications. More specifically, an effective combination of weight to strength ratio, advanced corrosion resistance, and high electrical and

thermal conductivities makes aluminum alloys suitable for lightweight clad sheets for BEV batteries. In many cases, Al-clad Al sheets are fabricated with a clad layer of AA4xxx (Al-Si series) and a core layer of AA3xxx (Al-Mn series) alloy due to the high corrosion resistance and strength [4,5], respectively, of these constituents. Thus, using Al-clad Al sheets for BEV batteries can drive weight reduction, increased lifetimes, and improved performance of the cooling system due to these combined properties.

Likewise, in the manufacture of efficient battery system components, the need to join of Al-clad Al sheets is unavoidable. Several researchers have demonstrated conventionally joined Al-clad Al sheets using brazing [6,7]. However, during brazing, the amount of heat generation raises the temperature of the material to the annealing temperature of the target alloys, leading to reduced mechanical strength and thermal conductivity [8]. Sometimes, the high brazing temperature (about 600°C) that is between the melting temperatures of the core and skin layers [9-11] causes sagging of the thin aluminum sheets. Thus, sagging resistance is also required to improve the mechanical strength and thermal conductivity of these materials [12-15]. In addition, joining Al-clad Al sheets without damaging the lamination between the core and skin layer of the clad sheet using conventional joining techniques can be extremely difficult. Therefore, a suitable joining technique to join Al-clad Al sheets is undoubtedly necessary.

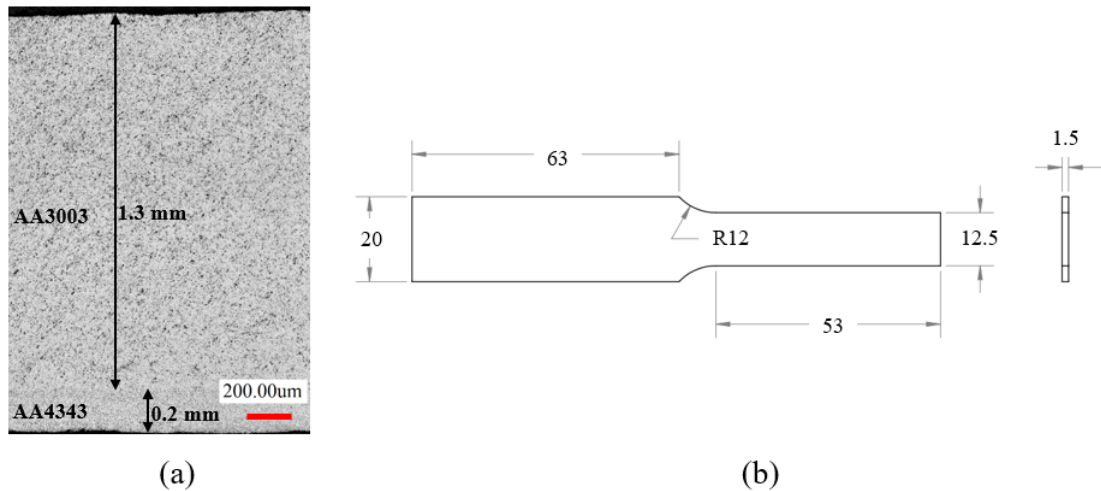
EAPJ could overcome several challenges related to brazing based on the ability of EAPJ to effectively join Al-clad Al thin sheets in the solid-state. Combining the effects of compressive plastic deformation, the thermal effect of resistance heating, and the athermal effect of an electric current [16-21] can effectively create rapid solid diffusion between two specimens to generate a joint in a relatively short time and at a relatively low temperature. The

effectiveness of EAPJ has been demonstrated in the successfully joining various combinations of similar and dissimilar materials [22-26].

The present work experimentally investigates the EAPJ of thin, cold-rolled Al-clad Al sheets developed for BEV battery casing applications. In EAPJ, an electric current and a compressive load with a constant displacement rate are simultaneously applied to the Al-clad Al sheets. Microstructure analysis and mechanical tests are performed on the EAPJed specimen to investigate the effectiveness of EAPJ.

## 4.2 EXPERIMENTAL SET-UP

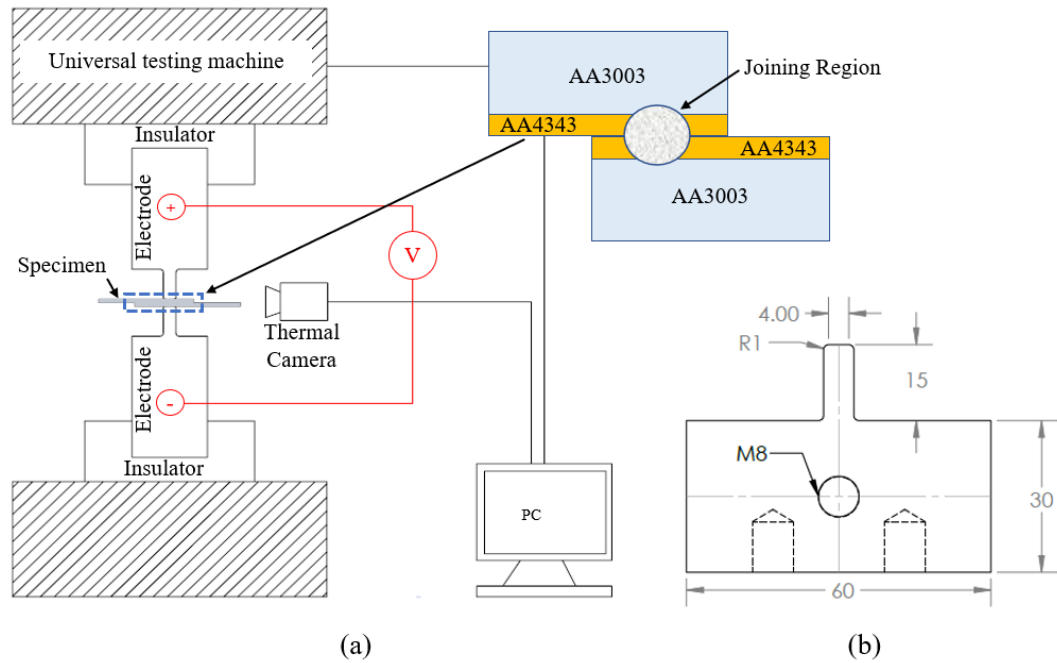
Cold-rolled bi-layer Al-clad Al sheets (1.5 mm thickness) consist of a core of AA3003 (1.3 mm thickness) and a clad layer of AA4343 (0.2 mm thickness) were used as received in EAPJ, as shown in Fig. 4.1(a). The chemical compositions (wt. %) of the AA3003 and AA4343 are listed in Table 4.1. Note that there is a significant difference in the Si content in



**Fig. 4.1.** Optical micrograph of the rolled Al-clad Al sheet used for joining and (b) the specimen design for EAPJ

the clad were (7.23 wt%) and core (0.33 wt%) alloys of the as-received material. Specimens for EAPJ fabricated in the shape half of an ASTM-E08 tensile specimen. The specimen shape and dimensions were selected to easily conduct tensile tests of the joined specimens, as shown in Fig. 4.1(b). Prior to EAPJ, the specimens were mechanically polished using 600-grit SiC sandpaper, followed by ethanol cleaning to remove residual oil from the surface.

A universal testing machine (DTU900-MH, Deakyong, South Korea) with custom-made fixtures was connected to a programmable power supply (Vadal SP-1000 U, Hyosung,



**Fig. 4.2.** (a) Schematic of the experimental set-up and (b) the design of electrode for EAPJ

**Table 4.1. Chemical compositions (wt %) of Al-clad Al sheets**

Material	Al	Si	Fe	Cu	Mn	Mg	Zn	Ti	
Core	AA3003	Bal.	0.33	0.54	0.14	1.11	0.01	0.02	0.004
Clad	AA4343	Bal.	7.23	0.33	-	-	-	-	0.02

South Korea) for EAPJ, as shown in Fig. 4.2(a). The Al-clad Al sheets were assembled in a lap joining configuration and placed between two electrodes so that the clad layers for both specimens were in contact with each other in the middle. The electrodes were designed with a flat tip width of 4 mm, which further corresponds to the target joint length of the EAPJed specimens, as depicted in Fig. 4.2(b).

During joining, a compressive pre-displacement (approximately 0.45 mm) at a displacement rate of 4 mm/min was applied to the specimen assembly to induce a pre-load of 6 kN prior to applying an electric current. This pre-loading helped avoid sparks, which may



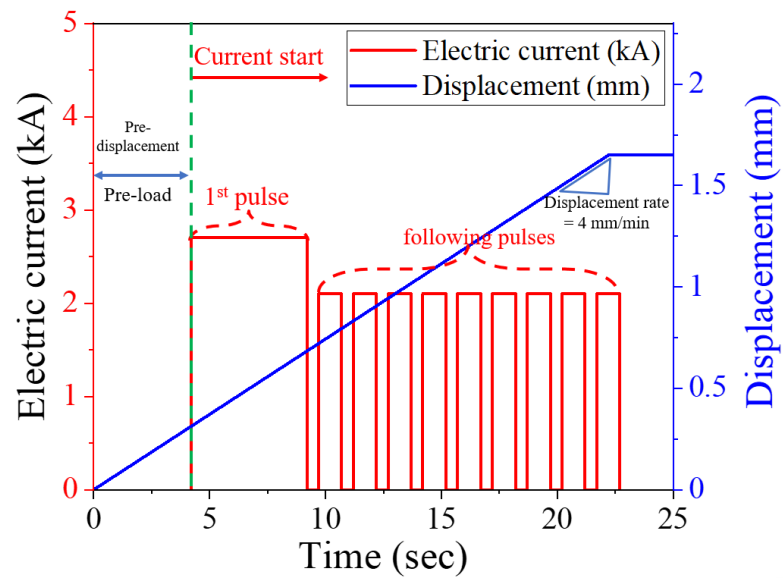
occur during the joining process if there is poor contact between the electrode and the specimen. When the pre-load of 6 kN was reached, a pulsed electric current, as described in Fig. 4.3, was applied to the joining region using the punches as electrodes, while the compressive displacement was continuously applied at the same displacement rate until the completion of joining. The detailed electric current parameters, which were selected based on the result of a preliminary parameter study, are listed in Table 4.2. Each experiment, with the parameters listed in Table 4.2, was repeated five times to confirm the repeatability of the results. Process responses, including axial compressive load and displacement, were recorded by a load cell (CSDH, Bongshin, South Korea) with a maximum capacity of 300 kN and a displacement sensor. In addition, one edge of the specimen assembly was painted with heat-resistant black paint to measure the temperature during EAPJ using an infrared thermal imaging camera (FLIR-T621, FLIR, Sweden).

After joining, the cross-section of the joint was ground, polished with a 0.004- $\mu\text{m}$  diamond suspension, and etched with Keller's reagent for optical microscopy (OM) with a laser scanning confocal microscope (LSCM, VK-X200, Keyence). Energy-dispersive X-ray spectroscopy (EDS; X-Max50, Horiba, Japan) using a scanning electron microscope (FE-SEM; SU5000, Hitachi, Japan) was used to investigate the elemental distribution across the joint interface of the EAPJ joint. Further, the cross-section of the joint was electropolished with a 10% perchloric acid in ethanol solution for electron backscatter diffraction (EBSD) studies (FE-SEM; Quanta 200F, FEI company, Czech Republic, EBSD; Digiview4, EDAX, USA). Finally, mechanical testing was carried out to characterize the mechanical performance of the joint in correlation with the joint microstructure. A microhardness measurement was also performed on the cross-section of the joint using a Vickers hardness tester (HM-100,

**Table 4.2. Compressive displacement and electric current conditions for EAPJ**

Case	Pre-load (kN) (Pre-displacement (mm))	Displacement* (mm)	First pulse		Following pulses (9 pulses)		Interval (sec)	Total joining time (sec)	Max. temperature (°C)
			Current (kA)	Duration (sec)	Current (kA)	Duration (sec)			
1									455
2									455
3	6 (0.45)	1.20	2.70	5	2.10	1	0.50	18.5	460
4									460
5									465

\* Displacement rate of 4 mm/min.



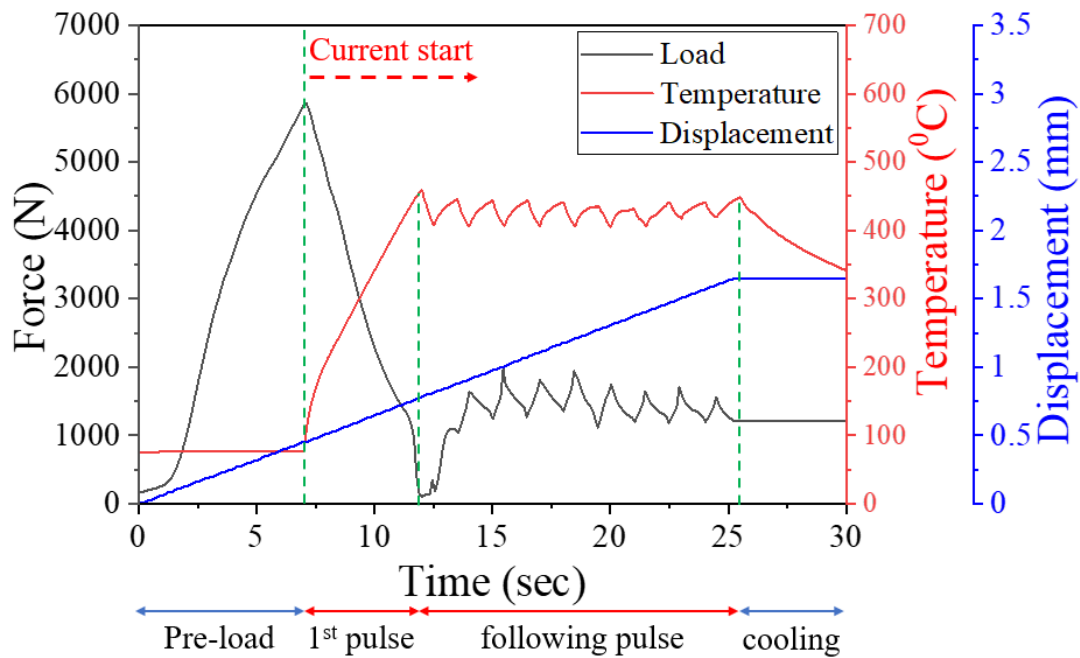
**Fig. 4.3.** Experimental conditions for applied current and compressive displacement

Mitutoyo, Japan) with an applied load of 0.098 N (10 gf) with a dwell time of 10 seconds. Finally, a lap shear tensile test was carried out with a cross-head speed of 1 mm/min to interrogate the fracture area and joint strength of the EAPJed Al-clad Al sheets.

### 4.3 RESULTS AND DISCUSSIONS

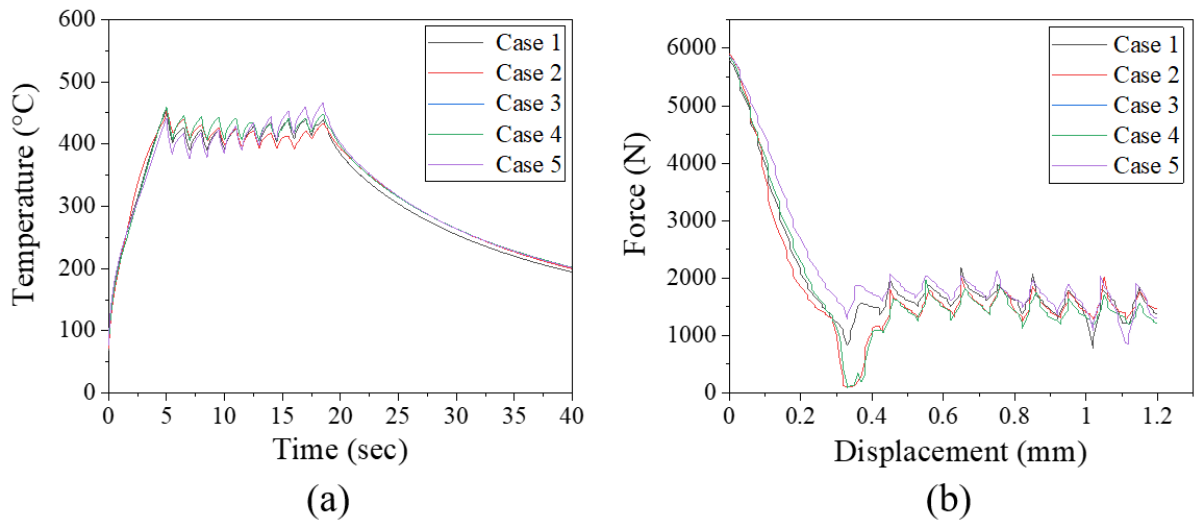
As expected, once the first pulse of electric current was applied to the joining area, the temperature rapidly increased to the target joining temperature, and the compressive load quickly decreased as the materials softened due to the elevated temperature. As shown in Fig. 4.4, the temperature then remained nearly constant (at approximately 460 °C) during the remaining portion of the pulsed electric current, enhancing the atomic diffusion between the materials until the completion of joining. Note that throughout the entire joining process, the temperature was definitively lower than the melting temperatures of the AA4343 clad layer (576 °C) and the AA3003 core (640 °C) [6,7]. After joining, the specimen was air-cooled to room temperature before it was taken out of the joining fixture. The process responses, including the peak temperature and compressive displacement histories, were recorded, as shown in Fig. 4.5.

The OM (Fig. 4.6(a)) of the cross section of the joint suggests that the joint was fabricated successfully by EAPJ. A magnified image of the marked region (green box) in Fig. 6(a) confirms the absence of obvious defects inside the joining region, as shown in Fig. 4.6(b). The absence of dendritic structures of melted aluminum in the middle and sides of the joint confirms that the joining has been performed in the solid-state. The length of the joining area is approximately 4.9 mm, which is slightly longer than the length of the flat area of the electrode tip (4.0 mm). The final measured thickness of the joint is reduced significantly from 3 mm to 1.35 mm, the same as the calculated value from the set parameters. Combining these observations from OM, it can be concluded that the materials underwent severe compressive straining under the designated parameter during EAPJ.



**Fig. 4.4.** Compressive displacement, electric current and corresponding load during EAPJ

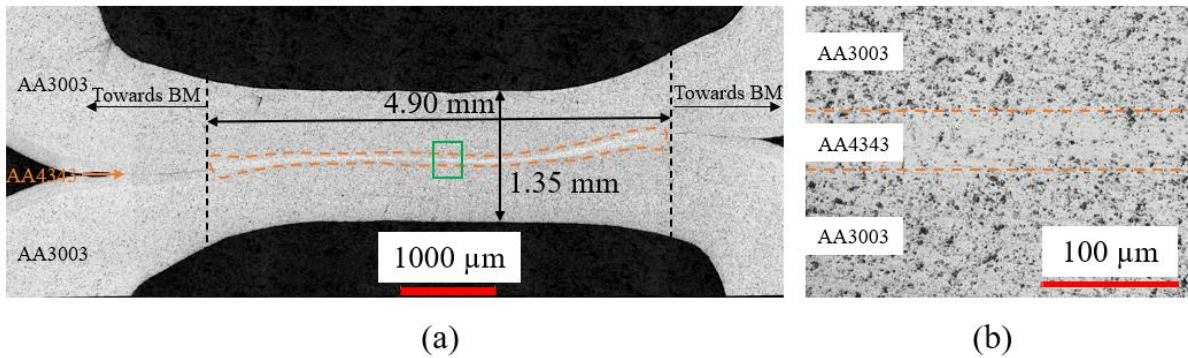
The EDS elemental maps of the SEM images of the as-received material (Fig. 4.7(a)) and the EAPJed region (Fig. 4.7(b)) provide a general understanding of the change to the silicon (Si) distribution from the clad to the core during joining. The elemental mapping of Al and Si particles in Fig. 4.7(a) shows uniformly distributed Si particles inside the Al matrix of the clad layer. Additionally, as expected from the chemical composition, the amount of Si inside the core alloy of the as-received specimen is significantly low (Figs. 4.7(a1) and (a2)). In contrast, the elemental maps of Si and Al at the joining region show a scattered distribution of Si particles inside the Al matrix of the core after EAPJ, as illustrated in Figs. 4.7(b1) and (b2). The Si map further confirms that the Si movement occurred in both directions (up and down) from the clad layer region of the joint. The enhanced mobility of atoms under EAPJ conditions of compressive deformation, elevated temperature, and athermal effect of electric



**Fig. 4.5.** Process response during EAPJ: (a) measured peak temperature and (b) compressive displacement history

current [16-26] could explain this change in the distribution of Si particles.

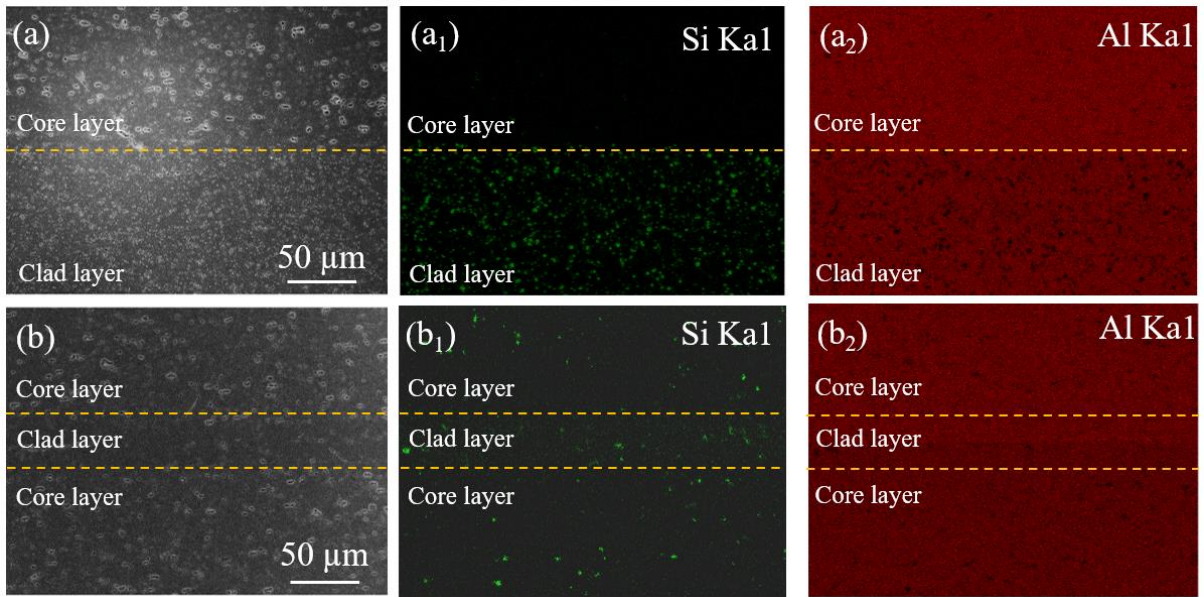
Furthermore, the presence of second phase particles inside the joining area is also apparent from the higher magnification SEM image (Fig. 4.8(b)) captured from the marked region (yellow box) of Fig. 4.8(a). The presence of Al<sub>6</sub> (Mn, Fe) precipitates in different shapes and sizes in AA3003 and Si-rich particles in AA4343, which is common for these alloys irrespective of processing conditions [6,27-29], were observed. Additionally, a few different types of precipitates were observed in the joining area of the clad layers (P3, P4) and core layers (P1, P2, P5), as shown in Fig. 4.8 and listed in Table 3. After EAPJ, the clad layer showed the formation of Al (1% Si), while other types of precipitates, including  $\alpha$  – Al (Fe, Mn) Si and  $\alpha$  – AlMnSi, were observed inside the core layers near the joint interface. The Si-induced precipitation in the core near the joint interface (the clad) confirms the Si particle



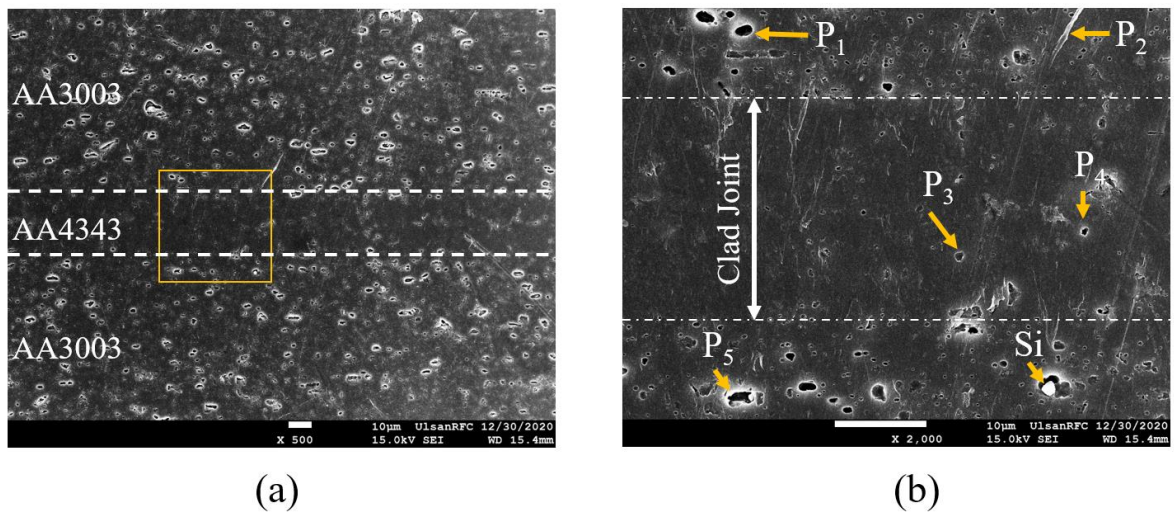
**Fig. 4.6.** (a) Typical cross-section of EAPJ collage and (b) higher magnification view of the green box region in (a)

diffusion from the clad layer to the core, as the original core alloy (AA3003) has a significantly low Si content.

EBSD analysis of the grain structure of the Al-clad Al sheet before and after EAPJ was carried out with the help of inverse pole figure (IPF) maps and misorientation angle distribution charts (Figs. 4.9 and 10). In Figs. 4.9 (b), (c), and (e), the low angle grain boundaries (LABs) from  $3^\circ$  to  $15^\circ$  and the high angle grain boundaries (HABs) greater than  $15^\circ$  are designated by white and black lines, respectively. Before EAPJ, the microstructure of the AA3003 core consists of elongated grains aligned parallel to the rolling direction (RD) (Fig. 4.9(b)), and that of the AA4343 clad is composed of equiaxed grains (Fig. 4.9(c)). Region 2 in Fig. 4.9(c) includes the interface of clad and core alloy, where a clear interfacial boundary (marked with a black dashed line) can be observed, showing the metallurgical bonding between the clad and the core of the as-received bi-layer clad sheet. After EAPJ, the microstructure consisted of elongated grains and subgrains in both the core (AA3003) and significant compressive strain of about 55% was applied to the specimen assembly. The grain became elongated in the perpendicular direction of the compressive strain and became thinner



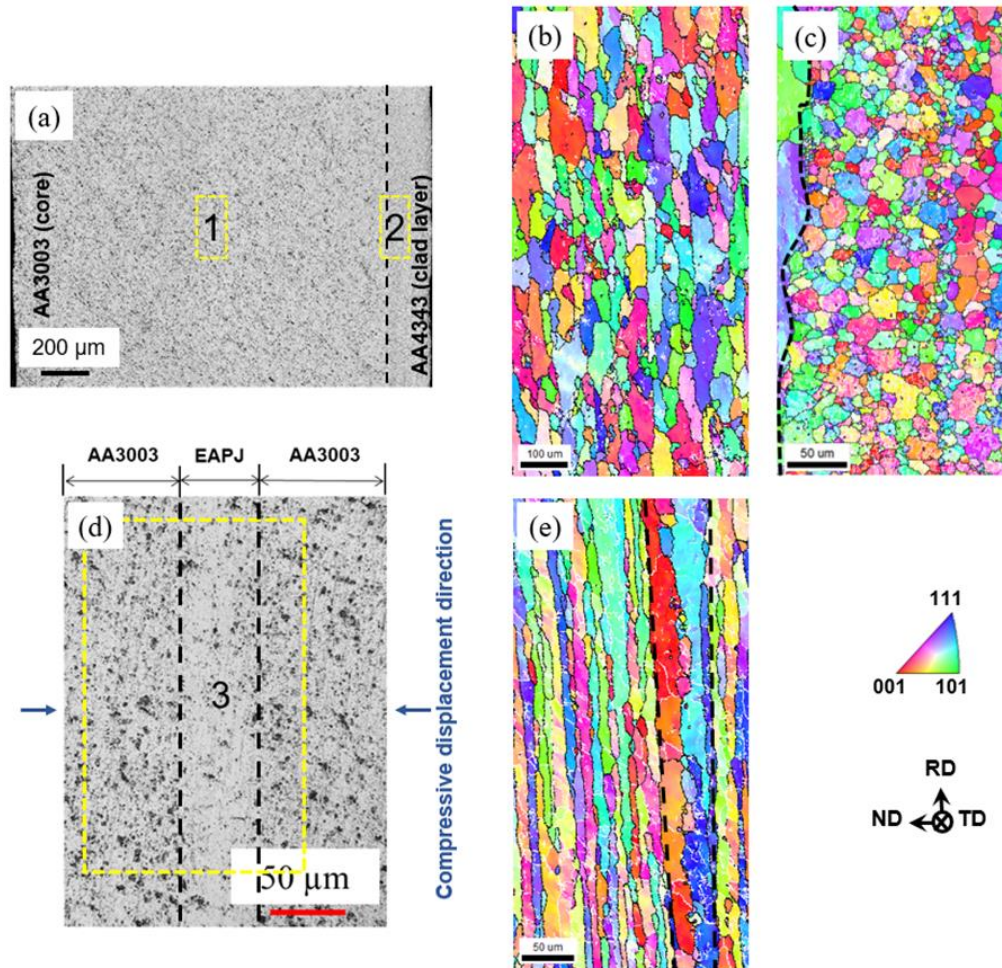
**Fig. 4.7.** EDS maps of Al and Si particles in (a) as-received and (b) EAPJed Al-clad Al sheets



**Fig. 4.8.** SEM micrographs of (a) the EAPJ region and (b) a magnified view of the region

marked by the yellow box in (a)

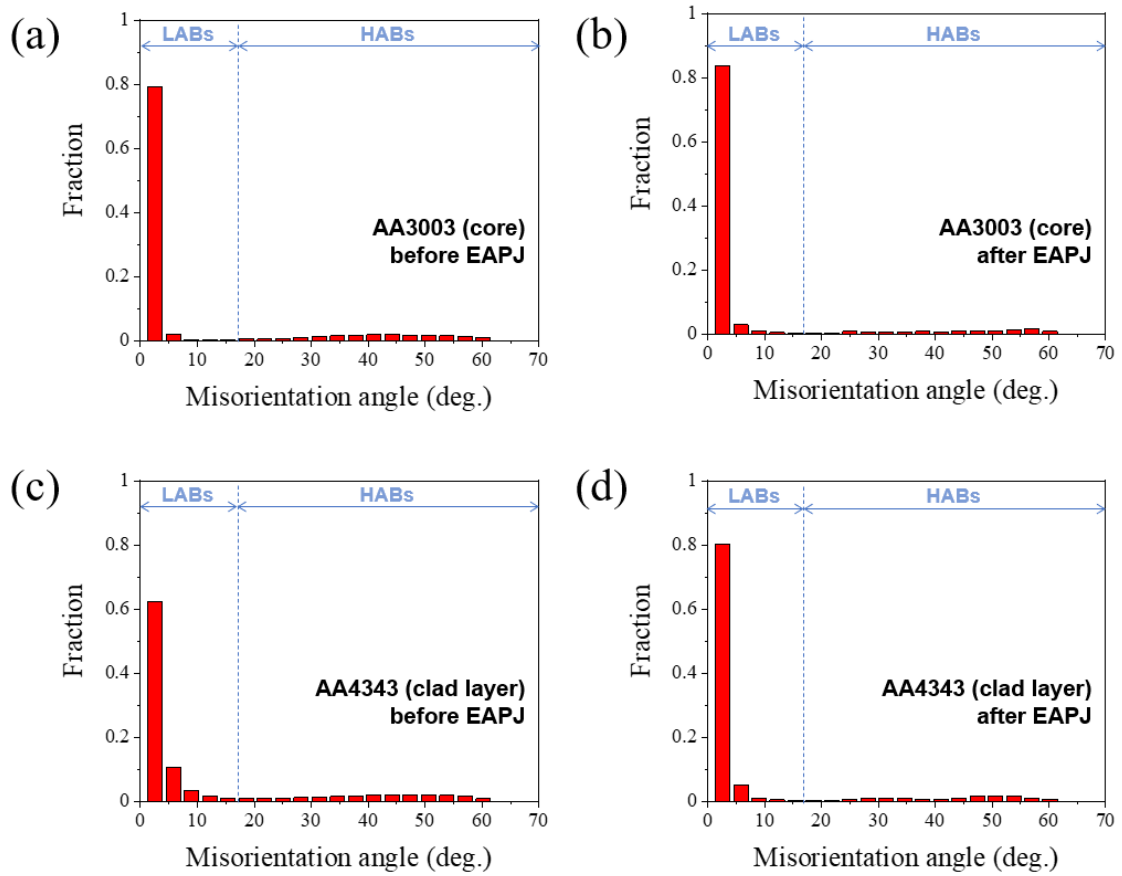
with subgrain structures due to a large compressive deformation. In the misorientation clad (AA4343), as shown in Fig. 4.9(e). The thickness of a sheet was 1.5 mm before EAPJ.



**Fig. 4.9.** (a) EBSD locations marked in the OM image of the as-received material (core (1), clad (2)), and inverse pole figure (IPF) maps for (b) marked region 1 and (c) marked region 2. (d) EBSD locations marked in the OM image after EAPJ, and (e) IPF map for marked region 3

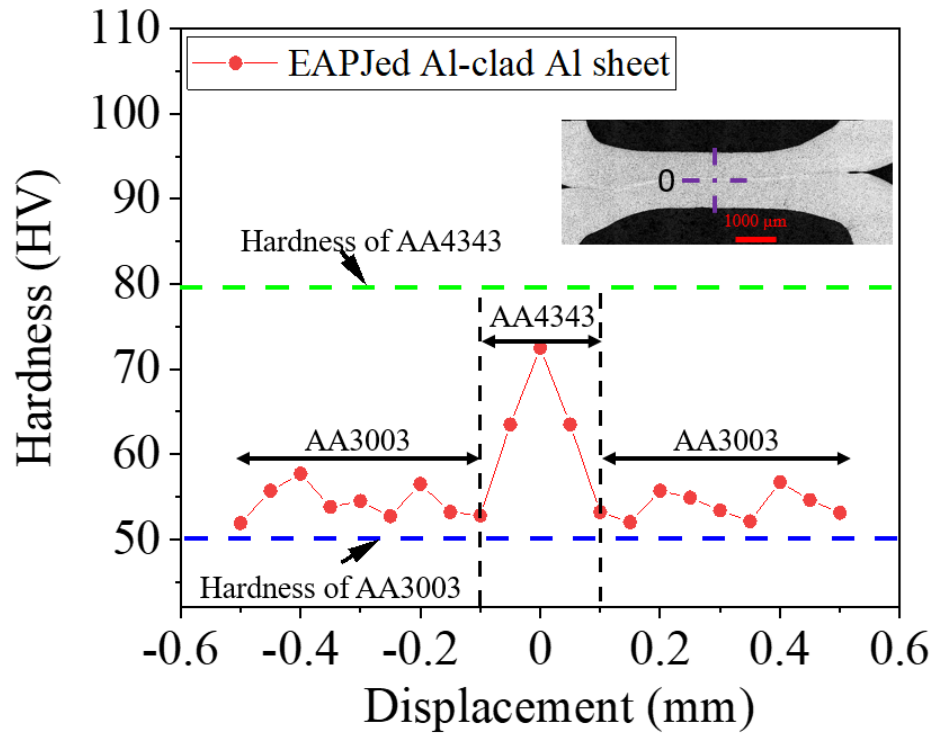
After EAPJ, the thickness of the joint of two sheets is 1.35 mm, which indicates that a distribution chart shown in Fig. 4.10, the LABs after EAPJ slightly increased in the core and significantly increased in the clad compared to those before EAPJ. This result implies that subgrain boundaries gradually increased during EAPJ. The elongated grain structure and high level of LABs after EAPJ can be explained by the fact that the compressive deformation was continuously applied until the final moment of joining, as described in Fig. 4.3.





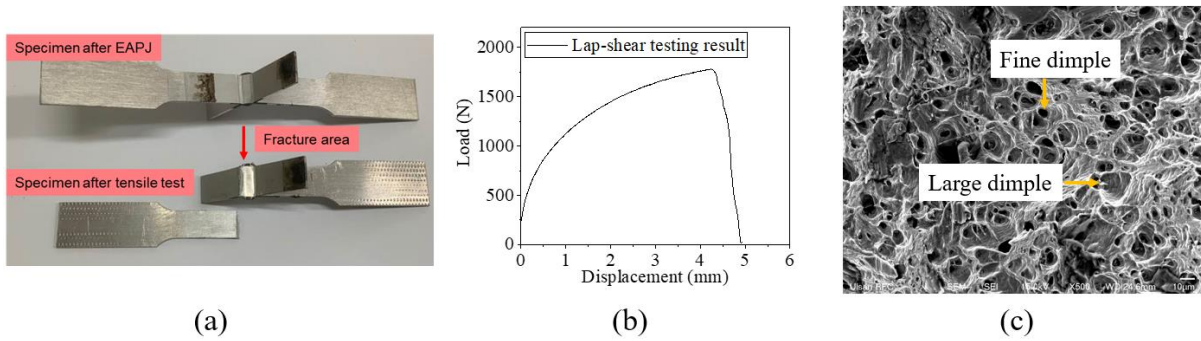
**Fig. 4.10.** Misorientation-angle distribution chart of (a) AA3003 before EAPJ, (b) AA3003 after EAPJ, (c) AA4343 before EAPJ, and (d) AA4343 after EAPJ

The microhardness distribution along the thickness of the EAPJ joint is shown in Fig. 4.11. The microhardness values of the core and clad layer of the as-received specimen are measured to be 50.20 HV and 79.40 HV, respectively, as individually marked with blue and green dashed lines in Fig. 4.11. The center of the EAPJ region is marked with the purple



**Fig. 4.11.** Vickers hardness profile of the cross-section of a EAPJed specimen along with the blue dashed line in the inset picture

dashed lines; the intersection point of these two was set as 0 mm, as reflected in the hardness data. The microhardness of the AA4343 clad slightly decreased compared to the as-received clad layer (79.40 HV to 72.50 HV). Generally, the LABs are closely related to dislocation density. In the AA4343 core, the fraction of LABs after EAPJ was higher than that before EAPJ, as shown in Figs. 4.10(c) and (d), indicating the existence of other factors lowering microhardness. The grain size after EAPJ is significantly higher than it was before EAPJ. Therefore, the decreased microhardness of the clad layer after EAPJ may be explained by the increased grain size. In the case of the AA3003 core, the fractions of LABs before and after EAPJ show similar values, as shown in Figs. 4.10(a) and (b), indicating that dislocation had an insignificant effect on the hardness. Instead, the increasing amount of Si particles in the



**Fig. 4.12.** (a) EAPJed specimen before and after fracture, (b) lap-shear testing result, and (c) the fracture surface of tensile tested specimens

**Table 4.3. Precipitates inside and in the vicinity of the clad layer’s joining area, as marked P1 – P5 in Fig. 4.8(b)**

Points	Compositions (at%)	Precipitates
P <sub>1</sub>	Al: 82.84 Si: 4.96 Mn: 3.89 Fe: 8.31	$\alpha$ – Al (Fe, Mn) Si
P <sub>2</sub>	Al: 95.02 Si: 4.84 Mn: 0.14	$\alpha$ – AlMnSi
P <sub>3</sub>	Al: 96.52 Si: 3.48	Al (1% Si)
P <sub>4</sub>	Al: 96.54 Si: 3.46	Al (1% Si)
P <sub>5</sub>	Al: 84.86 Si: 4.54 Mn: 5.24 Fe: 5.37	$\alpha$ – Al (Fe, Mn) Si

AA3003 cores in the joining area (Figs. 4.7 and 4.8) may explain the increase in the microhardness of the core region. The enhancement and reduction of the microhardness related to the particular core and clad materials can be linked to the changes in grain size,

distribution of Si particles, and the formation of secondary phase particles, as discussed earlier with the SEM-EDS and EBSD analysis.

The lap-shear tensile test was conducted to evaluate the joint strength of the EAPJed Al-clad Al sheets. Specimen images before and after conducting the lap-shear tensile test are shown in Fig. 4.12(a). The load-displacement curve is used to evaluate the strength of the joint, as shown in Fig. 4.12(b). The result cannot be used to identify the interfacial fracture strength of the joint directly. However, the EAPJed specimen was fractured at the base material near the joining area during the uniaxial lap-shear tension test, confirming that the load for the interfacial fracture of the joint ( $F_{\text{joint}}$ ) is higher than the measured tensile fracture load ( $F_{\text{tensile}}$ ) ( $F_{\text{tensile}} \leq F_{\text{joint}}$ ). Therefore, the joint interfacial strength ( $\tau_{\text{joint}}$ ) is at least higher than the shear stress calculated by the joint area and the tensile fracture load ( $F_{\text{tensile}}/A_{\text{joint}} \leq \tau_{\text{joint}}$ ), where  $A_{\text{joint}}$  is the joint area. Therefore, the lower boundary of the joint interfacial strength of the EAPJed Al-clad Al sheet is calculated to be 109.88 MPa. The fracture surface of the tested specimen (Fig. 4.12(c)) indicates the ductile mode of fracture at the base material. Thus, the EAPJ of rolled Al-clad Al sheets was performed a good joint without deterioration of joint strength in a remarkably short time.

#### **4.4 CONCLUSIONS**

Solid-state lap joining of the cold-rolled Al-clad Al sheets has been demonstrated without significant defects to the clad sheets by EAPJ, which was conducted by simultaneously applying electric current and compressive displacement. The analysis of microstructural properties through OM, SEM, EDS, and EBSD indicated the presence of deformed elongated grains and Si particles diffused from the clad to the core layers during joining. Furthermore, the change in microhardness is in good agreement with the microstructure changes induced by EAPJ without joint strength deterioration of the Al-clad Al sheet. This work will contribute to the manufacture of a cost-effective and lightweight battery system for BEVs using Al-clad Al sheets.

## **ACKNOWLEDGEMENT**

This work was supported by the National Research Foundation of Korea (NRF) grant funded by the Korea government (MSIT) (No. 2019R1A2C2009939 and No. 2020R1A5A6017701). This work was also supported by the Technology Innovation Program (No. 20006974) funded by the Ministry of Trade, Industry & Energy (MOTIE, Korea). In addition, M-J.K. was supported by the Industrial Strategic Technology Development Program (No. 20003937) funded by the Ministry of Trade, Industry & Energy (MOTIE, Korea).

## REFERENCES FOR CHAPTER IV

- [1] J.C.Benedyk, 3 - Aluminum alloys for lightweight automotive structures, *Materials, Design and Manufacturing for Lightweight Vehicles* (2010) 79-113. <https://doi.org/10.1533/9781845697822.1.79>.
- [2] E. Ghassemieh, *Materials in Automotive Application, State of the Art and Prospects*, 2011. <https://doi.org/10.5772/13286>.
- [3] Z. Rao, S. Wang, A review of power battery thermal energy management, *Renewable and Sustainable Energy Reviews* 15(9) (2011) 4554-4571. <https://doi.org/10.5772/13286>.
- [4] G.J. Marshall, R.K. Bolingbroke, A. Gray, Microstructural control in an aluminum core alloy for brazing sheet applications, *Metallurgical Transactions A* 24(9) (1993) 1935-1942. <https://doi.org/10.1007/BF02666328>
- [5] Z. Yuan, Y. Tu, T. Yuan, Y. Zhang, Y. Huang, Effect of post-brazing heat treatment on the corrosion mechanism of sandwich multi-layered aluminium sheets, *Vacuum* 183 (2021). <https://doi.org/10.1016/j.vacuum.2020.109781>
- [6] J. Lacaze, S. Tierce, M.C. Lafont, Y. Thebault, N. Pébère, G. Mankowski, C. Blanc, H. Robidou, D. Vaumousse, D. Daloz, Study of the microstructure resulting from brazed aluminium materials used in heat exchangers, *Materials Science and Engineering: A* 413-414 (2005) 317-321. <https://doi.org/10.1016/j.msea.2005.08.187>
- [7] S. Tierce, N. Pébère, C. Blanc, G. Mankowski, H. Robidou, D. Vaumousse, J. Lacaze, Solidification and phase transformations in brazed aluminium alloys used in automotive heat exchangers, *International Journal of Cast Metals Research* 18(6) (2013) 370-376. <https://doi.org/10.1179/136404605225023144>

- [8] L. Long, Q. Pan, M. Li, J. Ye, Y. Sun, W. Wang, Y. Luo, X. Li, Z. Peng, S. Liu, Study on microstructure and mechanical properties of 3003 alloys with scandium and copper addition, *Vacuum* 173 (2020). <https://doi.org/10.1016/j.vacuum.2019.109112>.
- [9] C. Xia, Y. Li, U.A. Puchkov, S.A. Gerasimov, J. Wang, Microstructure and phase constitution near the interface of Cu/Al vacuum brazing using Al–Si filler metal, *Vacuum* 82(8) (2008) 799-804. <https://doi.org/10.1179/136404605225023144>.
- [10] J.-c. Zhang, D.-y. Ding, W.-l. Zhang, S.-h. Kang, X.-l. Xu, Y.-j. Gao, G.-z. Chen, W.-g. Chen, X.-h. You, Effect of Zr addition on microstructure and properties of Al–Mn–Si–Zn-based alloy, *Transactions of Nonferrous Metals Society of China* 24(12) (2014) 3872-3878. [https://10.1016/S1003-6326\(14\)63545-7](https://10.1016/S1003-6326(14)63545-7)
- [11] H. Jin, M.S. Kozdras, B.S. Amirkhiz, S.L. Winkler, Liquid–Solid Interaction in Al-Si/Al-Mn-Cu-Mg Brazing Sheets and Its Effects on Mechanical Properties, *Metallurgical and Materials Transactions A* 49(7) (2018) 3091-3107. <https://doi.org/10.1007/s11661-018-4670-8>.
- [12] A.N. Akira Kawahara, Takeyoshi Doko, Development of Aluminum Alloy Fin Stock for Heat Exchangers Using Twin-Roll Continuous Casting Method, *Furukawa Review* (2003) 81-87. <https://www.furukawa.co.jp/review/fr024/fr2416.pdf>.
- [13] J. Qin, S.-B. Kang, J.-H. Cho, Sagging mechanisms in the brazing of aluminum heat exchangers, *Scripta Materialia* 68(12) (2013) 941-944. <http://dx.doi.org/10.1016/j.scriptamat.2013.02.039>.
- [14] Z. Xu, L. Peng, X. Lai, Electrically assisted solid-state pressure welding process of SS 316 sheet metals, *Journal of Materials Processing Technology* 214(11) (2014) 2212-2219. <http://dx.doi.org/10.1016/j.jmatprotec.2014.04.022>.



- [15] M. Way, J. Willingham, R. Goodall, Brazing filler metals, *International Materials Reviews* 65(5) (2019) 257-285. <https://doi.org/10.1080/09506608.2019.1613311>.
- [16] J.-H. Roh, J.-J. Seo, S.-T. Hong, M.-J. Kim, H.N. Han, J.T. Roth, The mechanical behavior of 5052-H32 aluminum alloys under a pulsed electric current, *International Journal of Plasticity* 58 (2014) 84-99. <http://dx.doi.org/10.1016/j.jmatprotec.2014.04.022>.
- [17] K. Hariharan, M.-G. Lee, M.-J. Kim, H.N. Han, D. Kim, S. Choi, Decoupling Thermal and Electrical Effect in an Electrically Assisted Uniaxial Tensile Test Using Finite Element Analysis, *Metallurgical and Materials Transactions A* 46(7) (2015) 3043-3051. <https://doi.org/10.1007/s11661-015-2879-3>.
- [18] J.-W. Park, H.-J. Jeong, S.-W. Jin, M.-J. Kim, K. Lee, J.J. Kim, S.-T. Hong, H.N. Han, Effect of electric current on recrystallization kinetics in interstitial free steel and AZ31 magnesium alloy, *Materials Characterization* 133 (2017) 70-76. <https://doi.org/10.1016/j.matchar.2017.09.021>.
- [19] A. Ghiotti, S. Bruschi, E. Simonetto, C. Gennari, I. Calliari, P. Bariani, Electroplastic effect on AA1050 aluminium alloy formability, *CIRP Annals* 67(1) (2018) 289-292, <https://doi.org/10.1016/j.cirp.2018.04.054>
- [20] M.-J. Kim, S. Yoon, S. Park, H.-J. Jeong, J.-W. Park, K. Kim, J. Jo, T. Heo, S.-T. Hong, S.H. Cho, Y.-K. Kwon, I.-S. Choi, M. Kim, H.N. Han, Elucidating the origin of electroplasticity in metallic materials, *Applied Materials Today* 21 (2020). <https://doi.org/10.1016/j.apmt.2020.100874>.
- [21] T.A.N. Nguyen, H. Choi, M.-J. Kim, S.-T. Hong, H.N. Han, Evaluation of Efficiency of Electrically Assisted Rapid Annealing Compared to Rapid Induction Heat Treatment,

International Journal of Precision Engineering and Manufacturing-Green Technology (2021).  
<https://doi.org/10.1007/s40684-021-00382-z>.

[22] S.-T. Hong, Y.-F. Li, J.-W. Park, H.N. Han, Effectiveness of electrically assisted solid-state pressure joining using an additive manufactured porous interlayer, *CIRP Annals* 67(1) (2018) 297-300. <https://doi.org/10.1016/j.cirp.2018.04.062>.

[23] Y.-F. Li, H. Das, S.-T. Hong, J.-W. Park, H.N. Han, Electrically assisted pressure joining of titanium alloys, *Journal of Manufacturing Processes* 35 (2018) 681-686. <https://doi.org/10.1016/j.jmapro.2018.09.015>.

[24] Y.-F. Li, S.-T. Hong, H. Choi, H.N. Han, Solid-state dissimilar joining of stainless steel 316L and Inconel 718 alloys by electrically assisted pressure joining, *Materials Characterization* 154 (2019) 161-168. <https://doi.org/10.1016/j.matchar.2019.06.005>.

[25] M.-G. Jo, T.A.N. Nguyen, S. Park, J.-Y. Suh, S.-T. Hong, H.N. Han, Electrically Assisted Solid-State Joining of CrMnFeCoNi High-Entropy Alloy, *Metallurgical and Materials Transactions A* 51(12) (2020) 6142-6148. <https://doi.org/10.1007/s11661-02006035-1>.

[26] S. Zhang, K. Gao, S.-T. Hong, H. Ahn, Y. Choi, S. Lee, H.N. Han, Electrically assisted solid state lap joining of dissimilar steel S45C and aluminum 6061-T6 alloy, *Journal of Materials Research and Technology* 12 (2021) 271-282. <https://doi.org/10.1016/j.jmrt.2021.02.091>.

[27] Y.J. Li, L. Arnberg, Evolution of eutectic intermetallic particles in DC-cast AA3003 alloy during heating and homogenization, *Materials Science and Engineering: A* 347(1-2) (2003) 130-135. [https://doi.org/10.1016/S0921-5093\(02\)00555-5](https://doi.org/10.1016/S0921-5093(02)00555-5).

[28] D.T.L. Alexander, A.L. Greer, Solid-state intermetallic phase transformations in 3XXX aluminium alloys, *Acta Materialia* 50(10) (2002) 2571-2583. [https://doi.org/10.1016/S1359-6454\(02\)00085-X](https://doi.org/10.1016/S1359-6454(02)00085-X).

[29] X.-X. Dong, L.-J. He, G.-B. Mi, P.-J. Li, Dynamic investigation of the finite dissolution of silicon particles in aluminum melt with a lower dissolution limit, *Chinese Physics B* 23(11) (2014). <http://dx.doi.org/10.1088/1674-1056/23/11/110204>.

## CHAPTER V

### CONCLUSIONS AND PROJECT WORK

#### 5.1 CONCLUSIONS

In recent years, various studies have been conducted on electrically assisted manufacturing (EAM) utilizing a combination of thermal (resistance heating) and athermal effects of electric current. EA annealing, which is one of EAM methods, also uses the combination of thermal and athermal effects of electric current to enhance the efficiency of the process. Their advantages make EA annealing a promising energy-saving green technology. The quantification of the thermal and athermal contributions of electric current in EAM can be challenging. Consideration of the athermal effect is generally necessary to thoroughly describe the mechanical or microstructural behaviors under an electric current. Therefore, to design a commercialization ready EA annealing process, the athermal contribution of electric current during the process needs to be properly assessed.

The athermal contribution of electric current during EA annealing was assessed by comparing the performances of EA annealing and IHT. The calculation of reduction of dislocation density based on XRD measurement and the results of microstructural observation consistently suggest that EA annealing using the thermal effect of resistance heating and the athermal effect of electric current density can be more effective (energy-saving and cost-effective) compared to the conventional annealing process. However, as shown in the calculation of reduction of dislocation density and confirmed in the microhardness measurement, the 10% additional effectiveness of EA annealing can be beneficial in a certain

temperature range. At a relatively low temperature (or a low electric current density), EA annealing and IHT show nearly identical performance. Also, at an excessively high temperature, the thermal effect alone is able to induce nearly complete annihilation of dislocation density, thus, the practical advantage of EA annealing may diminish. Therefore, while EA annealing can be a very effective alternative to the conventional time-consuming annealing process with a furnace, in the design of EA annealing, electric current parameters and annealing temperature need to be carefully selected to properly benefit from the athermal contribution of electric current.

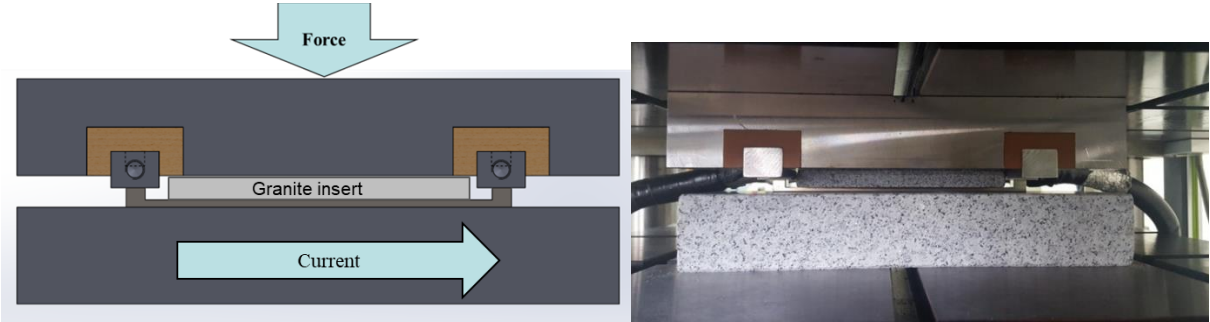
EAPJ is one of the EAM technologies. In EAPJ, an electric current is directly applied to the specimen during plastic compression. In comparison to conventional pressure joining, using resistance heating as a heat source provides several technical advantages. First, the workpieces can be heated rapidly and locally. As a result, the process time can be reduced and unnecessary thermal effects on the workpiece can be minimized. Also, the joining apparatus can be significantly simpler and cost-effective, as the need for a heating furnace can be eliminated. The concept of EAPJ also provides technical advantages over friction welding in the joining of bulk workpieces. By using resistance heating as a heat source, the need for complex rotation and brake systems can be eliminated. Also, since the heating of the interface can be continued during the final axial compression, process optimization is relatively easier. EAPJ is a promising technology which can bond similar or dissimilar various sheet and bulk metals with very short process time (just few seconds). However, nowadays studies on EAPJ of metal alloys are still limited and are mostly conducted on very thin foils.

The dissertation demonstrates the joining feasibility of HEA CrMnFeCoNi sheets, thin bi-layer cold-rolled aluminum-clad aluminum (Al-clad Al) sheets by EAPJ. The major achievements and findings of this dissertation of EAPJ can be summarized as follow:

- EAPJ was performed by applying plastic compressive deformation and electric current on CrMnFeCoNi HEA sheets. In a remarkably short time, a solid-state joint was successfully made without macro- and micro-cracks and compositional segregation. With the increase of electric current, the JZ changed from a deformed and partially recrystallized microstructure to a fully recrystallized one with grain growth. The mechanical properties of the JZ were investigated through uniaxial tensile tests and inverse finite element methods, and the obtained mechanical properties showed good agreement with the tendency of the experimentally measured hardness values. The HEA joined by EAPJ showed sound mechanical properties. It was confirmed that the EAPJ can overcome the disadvantages of fusion welding for HEA.
- Solid-state lap joining of the cold-rolled Al-clad Al sheets has been demonstrated without significant defects to the clad sheets by EAPJ, which was conducted by simultaneously applying electric current and compressive displacement. The analysis of microstructural properties through OM, SEM, EDS, and EBSD indicated the presence of deformed elongated grains and Si particles diffused from the clad to the core layers during joining. Furthermore, the change in microhardness is in good agreement with the microstructure changes induced by EAPJ without joint strength deterioration of the Al-clad Al sheet. This work will contribute to the manufacture of a cost-effective and lightweight battery system for BEVs using Al-clad Al sheets.

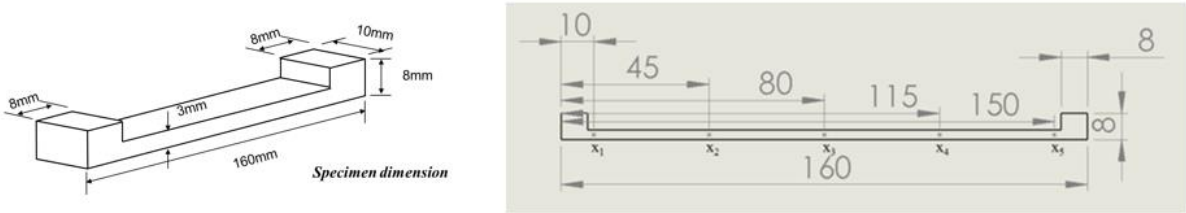
**5.2 INDUSTRIAL APPLICATION**

**5.2.1. EA flattening of 304 sheets**



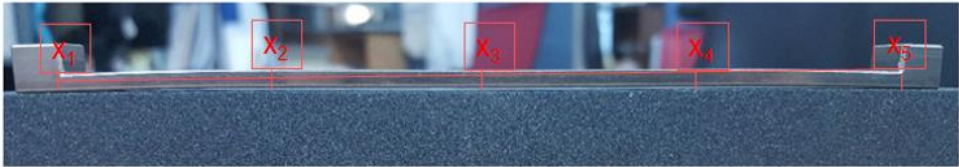
**Fig. 5.1.** Schematic and real experimental set-up

**Specimen**



Position of 5 measured point

**Before Test**



**After Test**



**Fig. 5.2.** Position of 5 measured points on the tested specimens

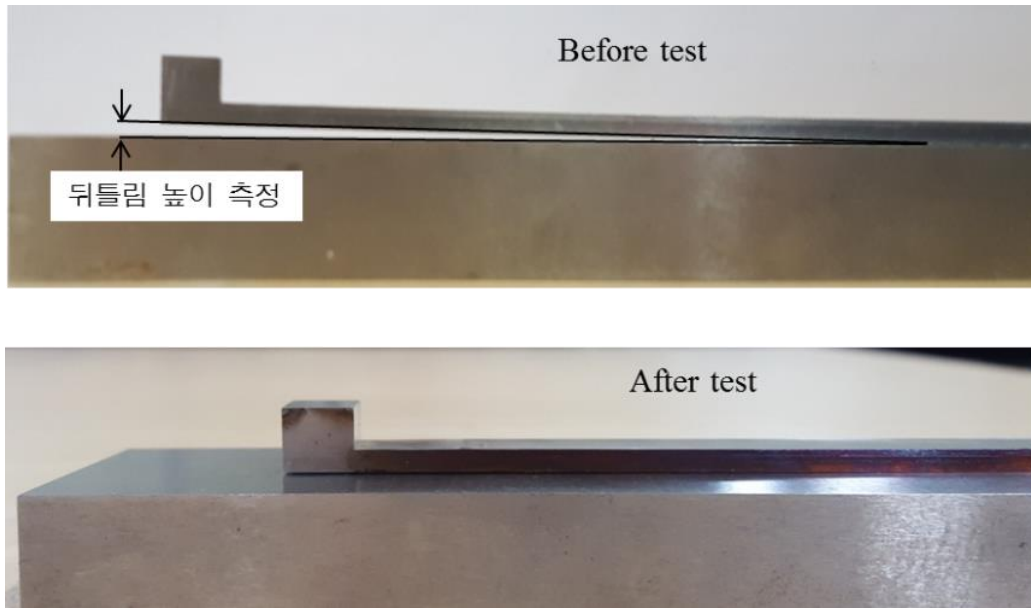


Fig. 5.3. The specimen before and after testing

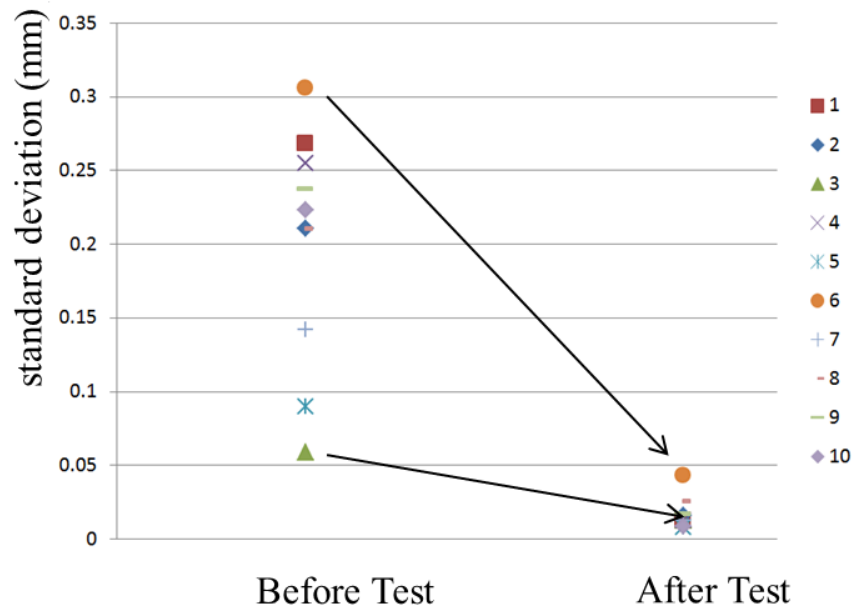


Fig. 5.4. The standard deviation before and after EA



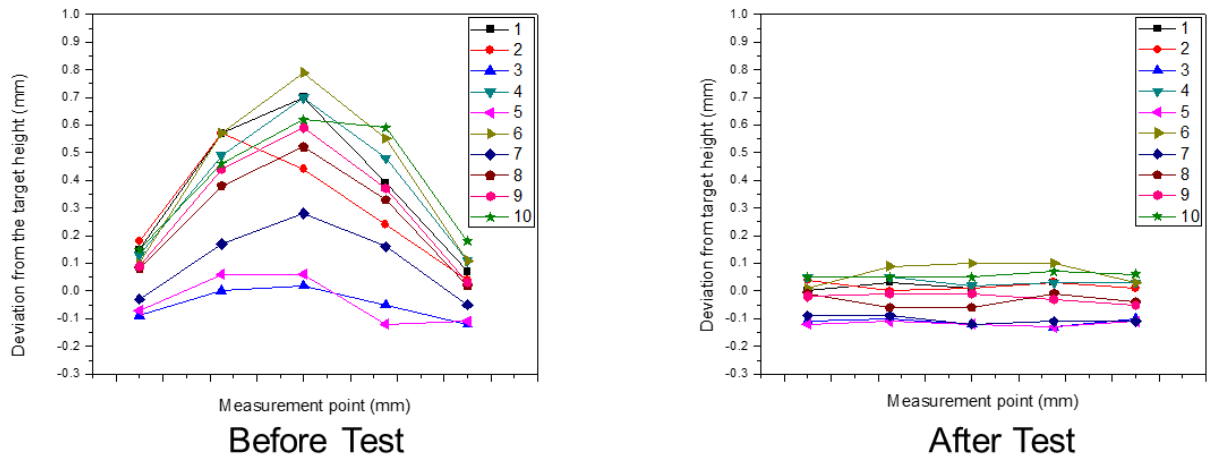


Fig. 5.5. Deviation from the target height of specimen before and after testing

### 5.2.2. Kimchi Container Bright Annealing

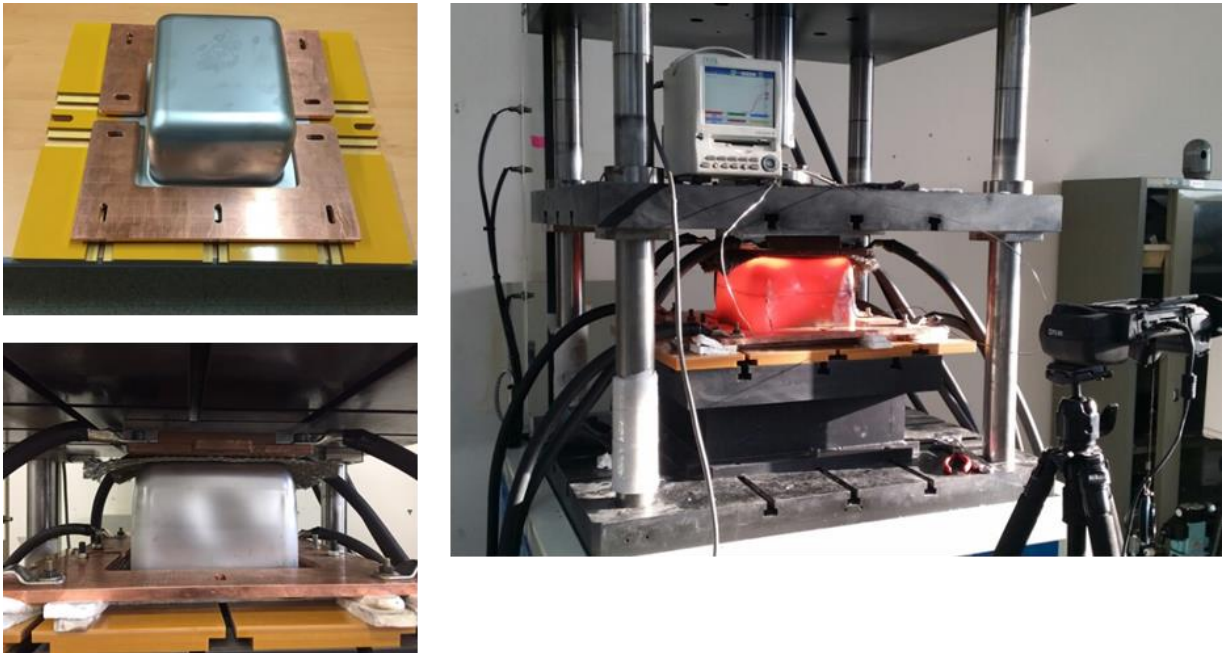
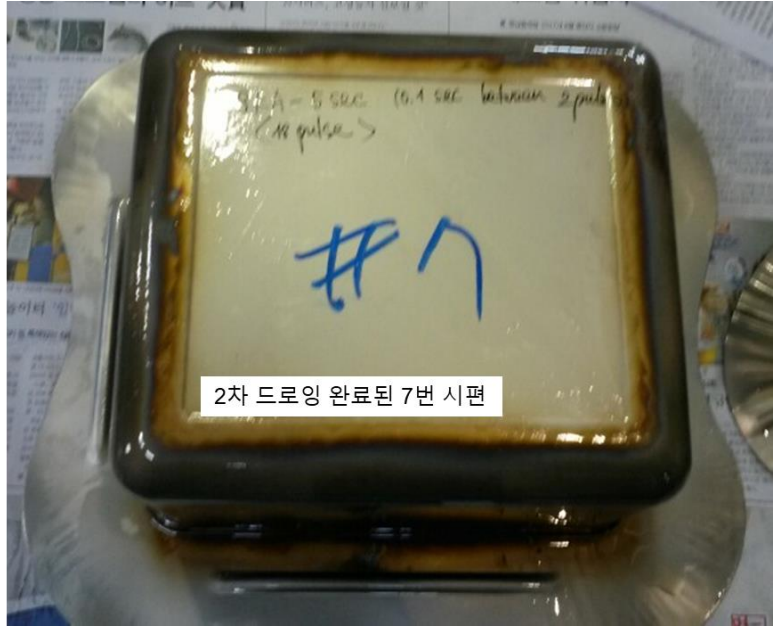
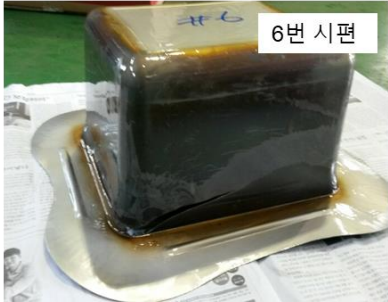


Fig. 5.6. The experimental set-up for bright annealing by electric current

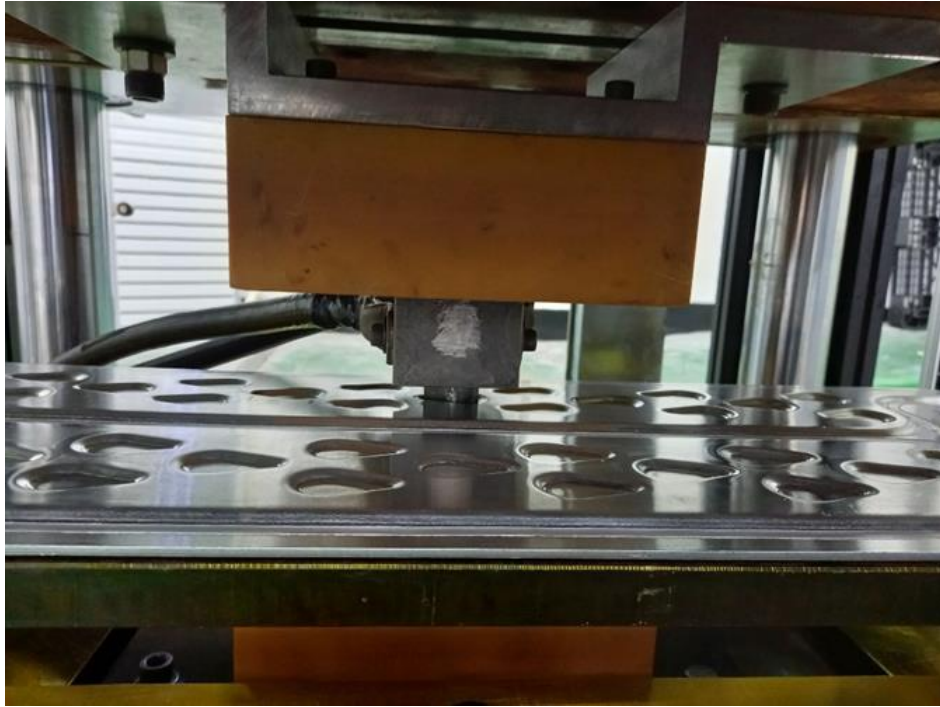


**Fig. 5.7.** The product after bright annealing by electric current

### 5.2.3. EAPJ of Al-clad Al sheets (apply for Battery Case)



**Fig. 5. 8.** The experimental set-up for battery case joining by EAPJ



**Fig. 5. 9.** The working area for each joint



**Fig. 5. 10.** The product after EAPJ